PHYSICAL REVIEW E **71**, 046201 (2005)

Experimental investigations of chaos-assisted tunneling in a microwave annular billiard

R. Hofferbert,[1,*] H. Alt,[1,†] C. Dembowski,[1,‡] H.-D. Gräf,[1] H. L. Harney,[2] A. Heine,[1,§] H. Rehfeld,[1,‖] and A. Richter[1]
[1]*Institut für Kernphysik, Technische Universität Darmstadt, D-64289 Darmstadt, Germany*
[2]*Max-Planck-Institut für Kernphysik, D-69029 Heidelberg, Germany*

(Received 21 October 2004; published 4 April 2005)

We present detailed investigations of the experimental signatures of chaos-assisted tunneling in the two-dimensional annular billiard, as already summarized in Phys. Rev. Lett. **84**, 867 (2000). We have performed analog experiments with two-dimensional, electromagnetic resonators allowing for a direct simulation of the corresponding quantum system. Spectra from a superconducting cavity with a high-frequency resolution are combined with electromagnetic intensity distributions of high spatial resolution experimentally determined using a normal conducting twin cavity. Thereby all eigenmodes were obtained with properly identified quantum numbers. Besides distributions of quasidoublet splittings, which serve as fundamental observables for the tunneling between whispering gallery types of modes, we also focus on the distributions of resonance widths of the doublets. These directly reflect the role of lifetime of certain modes in the tunneling process. Here, as theoretically expected, the class of so-called beach modes is found to play a particular role in mediating between regular and chaotic states to enhance the tunneling strength. This behavior is found in the spectrum and also in the structure of the wave functions.

DOI: 10.1103/PhysRevE.71.046201 PACS number(s): 05.45.Mt, 41.20.−q, 84.40.−x

I. INTRODUCTION

In [1] the first experimental observation of chaos-assisted tunneling in a quantum billiard has been presented. As subsequent studies of dynamical tunneling in ultracold atoms [2–8] have attracted a lot of attention, we provide in this article a more detailed presentation of the results of [1]. The mechanism of chaos-assisted tunneling has been studied in a vast literature of theoretical work during the last two decades [9–27], since it directly reflects the influence of chaotic phase-space structures of a classical system onto *single* states of its quantum counterpart. The common tunneling, usually defined as a classically forbidden passage of potential barriers [28–30], is hereby replaced by a classically also forbidden transition between dynamically distinct regions of the underlying phase space. This means that according to certain constants of motion—i.e., symmetries of the system—the considered classical particle is confined to restricted types of propagation and therefore trapped inside associated phase-space regions. In contrast to this, by virtue of the so-called "dynamical tunneling" [9] a quantum particle may leave these regions and travel into others. While in the case of a potential the tunneling probability depends on the size of the barrier and the energy of the particle, dynamical tunneling is solely governed by the coupling of distinct phase-space regions according to the motion of the particle.

If the classical transport between distinct regions in phase space is strongly influenced by a chaotic layer, the quantum system typically exhibits chaos-assisted tunneling [14]. Here, a very interesting case is given if a discrete symmetry of the system leads to *two* related, but dynamically distinct *regular* regions in phase space. Quantizing the associated tori leads to quasidegenerate states, so-called quasidoublets, just reflecting the symmetry of the system. Coupling between these distinct regions through a chaotic layer in phase space allows one in a direct manner to influence the splitting of those quasidoublets. The tunneling matrix element is hereby determined by the position of a quasidoublet in phase space relative to the chaotic layer.

The special role of chaotic phase-space structures in the tunneling phenomenon was investigated for the *annular billiard* [16] and for *two coupled quartic oscillators* [14]. In these studies a typical feature of chaos-assisted tunneling was found: namely, a characteristic crossing mechanism between quasidoublets and single chaotic states. Strong fluctuations and large amplitudes could be observed for the splittings when an external parameter of the system was varied in such a way that the chaotic part of phase space changes in size and form. In addition, the distribution of splittings could be very effectively modeled by Gaussian random matrices for systems with mixed classical dynamics. A couple of years ago, evidence for the existence of the new tunneling mechanism was also found in optical cavities [31,32], in deformed atomic nuclei [33], and in ultracold atoms [2–4].

All our investigations are based on analog experiments with two-dimensional, electromagnetic resonators (for an overview see [34]). As an ideal system for first experiments with superconducting microwave cavities, we used the two-dimensional annular billiard of [16] representing a paradigm for chaos-assisted tunneling in billiard systems [17–20,35]. While first results of this investigation have already been

---

[*] Present address: Max-Planck-Institut für Astronomie, D-69117 Heidelberg, Germany.

[†] Present address: Siemens Management Consulting, D-81541 München, Germany.

[‡] Present address: d-fine GmbH, D-60313 Frankfurt am Main, Germany.

[§] Present address: Fraunhofer EMI (Ernst-Mach-Institut), D-79104 Freiburg, Germany.

[‖] Present address: Ericsson GmbH, D-40547 Düsseldorf, Germany.

©2005 The American Physical Society

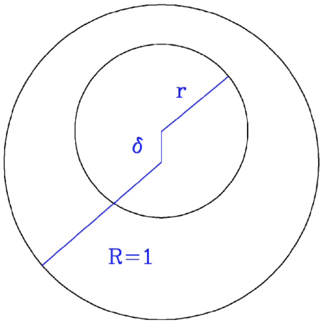

FIG. 1. (Color online) Geometry of the two-dimensional annular billiard. The eccentricity δ characterizes the center displacement of the two circles.

published in [1], the present paper describes the entire experiment and its analysis in detail.

The article is organized as follows: In Sec. II the classical system and the underlying phase-space structure are presented. We thereby provide information necessary for an understanding of its quantum counterpart. While the concentric configuration of the quantum annular billiard can be discussed analytically (as in Sec. III), our main interest is the presentation of the experiments with the nonconcentric annular billiard and of our experimental results. The microwave experiments and the investigation of the quasidoublet splittings are described in Sec. IV. The analysis of the data is given by Secs. V–VII, which contain details omitted in our previous Letter [1]. We conclude this article in Sec. VIII.

II. CLASSICAL ANNULAR BILLIARD AND ITS PHASE SPACE

The annular billiard [16,36] consists of two circles: one of radius $R=1$ defining the outer boundary and another with radius r inside the first one (with a center displacement δ) defining the inner boundary (see Fig. 1). The system is paradigmatic for the investigation of quantum chaotic effects that result from the possible configurations of the two-parameter family (r,δ). For any radius r of the inner circle and the particular eccentricity $\delta=0$ both circles are concentric. Only in this case do the number of degrees of freedom and the number of constants of motion of the propagating billiard particle (energy $\mathcal{E}$ and angular momentum $\vec{\mathcal{L}}$) coincide. This provides the regular case. Therefore, the one-parameter family $(r=\text{const},\delta)$ allows us to study the transition from regular to chaotic dynamics. If, on the other hand, the two properties r and δ are varied independently, the two-parameter family (r,δ) can be used to investigate avoided crossings and diabolic points [37].

A. Family $r+\delta=$const

In the following the particular one-parameter family with $r+\delta=$const, which is very suitable to study principal features of chaos-assisted tunneling, is introduced. Figure 2 displays how to construct geometrically the special family with $r+\delta=0.75$, which has been used in all following investigations.

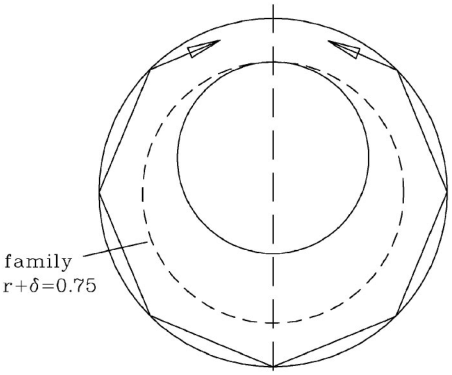

FIG. 2. The family of annular billiards with $r+\delta=0.75$ is very suitable to study chaos-assisted tunneling. The shown trajectories (arrows) are located right within the so-called whispering gallery region of the billiard.

At any possible configuration of this family, the inner circle is positioned inside the dashed limiting circle with radius $r'=0.75$ touching it in exactly one point. An attractive feature of the geometry lies in the fact that the chaoticity can be varied by changing r or δ without any influence on the motion between the dashed and outer circles. Inside this strip, the billiard particle does not interact with the inner circle and preserves its angular momentum after collisions with the outer circle. Since in this case the billiard "looks" rotationally symmetric for the particle, the dynamics is regular and possesses as many constants of motion (energy $\mathcal{E}$ and angular momentum $\vec{\mathcal{L}}$) as degrees of freedom. The strip is called the *whispering gallery* region of the billiard, where the caustic of the innermost whispering gallery trajectory is just the dashed circle with radius $r'=0.75$.

Another specific feature results from the reflection symmetry of the system (see also Fig. 2). It is possible to attach a direction of motion to the particular trajectories in the whispering gallery region, which can be derived from the sign of the corresponding angular momentum. As long as conservation of angular momentum applies (i.e., the inner circle is *not* hit), it is *not* possible to transform clockwise (cw) motion into counterclockwise (ccw) motion and vice versa (see Fig. 2). Thus, the reflectional symmetry of the system provides that whispering gallery trajectories (always pairs with positive and negative sense of motion) *cannot* be transformed into each other due to conservation of angular momentum.

The following subsection presents a more quantitative description of the ideas given here and introduces how to construct portraits of the corresponding phase-space. This will also demonstrate that all mentioned specific geometrical features create a phase-space structure, which is essential to observe chaos-assisted tunneling.

B. Construction of the phase space: Poincaré surfaces of section

To construct an adequate Poincaré surface of section of the classical phase space we use so-called Birkhoff coordinates. They preserve a given area of phase space under the

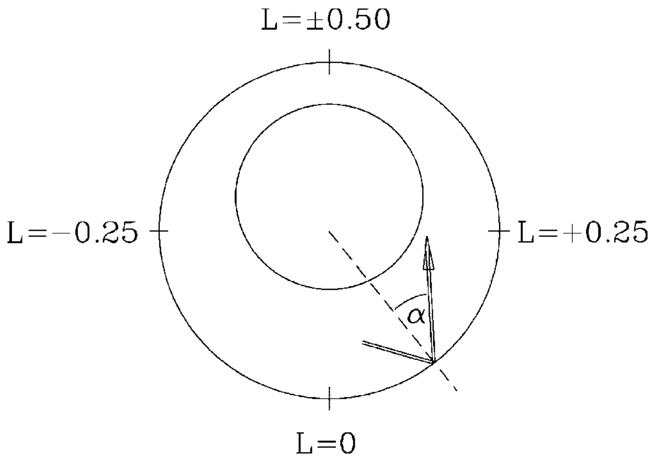

FIG. 3. Definition of the Birkhoff coordinates for the construction of adequate Poincaré surfaces of section of the classical phase space.

Hamiltonian flow; i.e., within Birkhoff coordinates Liouville's theorem for conservative systems [16,38] applies. The definition of the coordinates can be seen from Fig. 3. For every collision of the pointlike billiard particle with the outer circle the point of impact and the angle of reflection are considered as coordinates. The first coordinate L is the normalized arc length at the point of impact on the circumference of the outer circle. The second coordinate S is related to the direction of motion via the angle of reflection α through

$$S = \sin \alpha. \tag{1}$$

The quantity S has a very useful graphical interpretation. According to Fig. 3, the angular momentum $\vec{\mathcal{L}}$ of the reflected billiard particle is just given by

$$\vec{\mathcal{L}} = \vec{\mathcal{R}} \times \vec{\mathcal{P}} = |\vec{\mathcal{R}}||\vec{\mathcal{P}}|\sin \alpha \vec{e}_z = S\vec{e}_z. \tag{2}$$

This is a consequence of the normalization of the momentum, $|\vec{\mathcal{P}}| \equiv p = 1$, and the radius of the outer circle, $|\vec{\mathcal{R}}| \equiv R = 1$. The sign of the reflection angle serves as a definition of the sense of motion.

In the Poincaré surface of section, the conservation of the angular momentum ($S=\text{const}$) is geometrically indicated by horizontal, invariant curves in the LS plane. For eccentricities $\delta \neq 0$ this occurs only if the billiard particle does not collide with the inner circle—i.e., only for the whispering gallery trajectories. Any collision with the inner circle violates the conservation of angular momentum and results in chaotic motion.

However, in the particular case of the concentric billiard ($\delta = 0$), collisions with the inner circle have no influence on the angular momentum S. This characterizes the fully regular system. This feature implies the existence of two different types of regular orbits for the concentric billiard: First, there is the class of whispering gallery trajectories showing no collisions with the inner circle. Second, there is the class of orbits hitting alternately the inner and the outer circle ("starlike orbits").

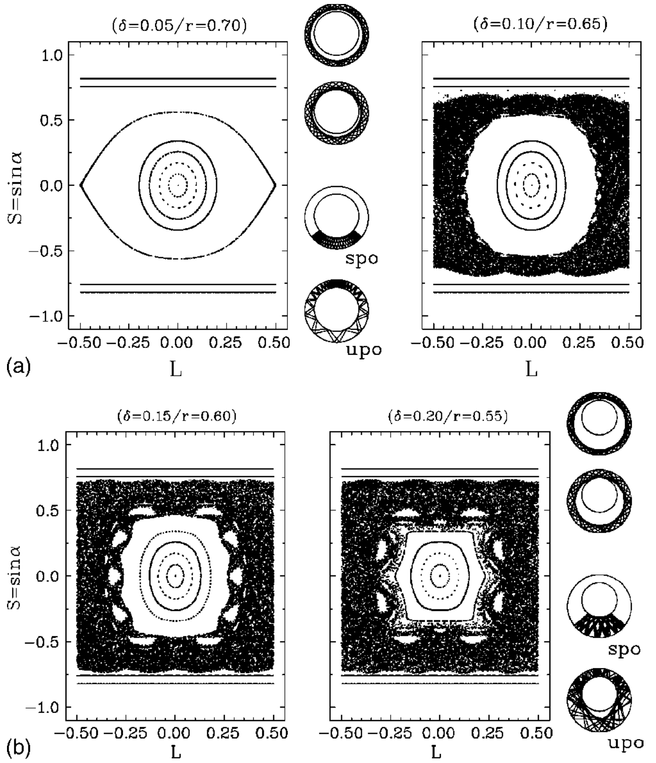

FIG. 4. Poincaré surfaces of section for the eccentric configurations $\delta = 0.05$, 0.10, 0.15, and 0.20 together with some examples of the generating trajectories in the configuration space. Here, the upper two trajectories are whispering gallery orbits (neutrally stable), while "spo" and "upo" label stable and unstable periodic orbits, respectively.

The two types of orbits show different behavior when one goes from the concentric billiard towards configurations with $\delta > 0$. This can be seen impressively in phase-space portraits using the Birkhoff coordinates L and S. In Fig. 4 the Poincaré surfaces of section for the eccentric configurations $\delta = 0.05, 0.10, 0.15, 0.20$ of the family $r + \delta = 0.75$ are given. They play a crucial role in the following investigations. These sections contain three parts: an island of stable motion in the center, a chaotic sea (which grows with increasing displacement δ), and—as expected—*two* invariant whispering gallery regions (defining "the outer coast"). The separated whispering gallery regions are located symmetrically with respect to the angular momentum $S=0$. Thus they differ by the sense of motion—i.e., the sign of the angular momentum of the billiard particle. Within Newtonian mechanics this is a conserved quantity.

For the eccentricities $\delta = 0.05$ and 0.20, Fig. 4 includes the trajectories which generate the structures in phase space.

Note that both the stable island in the center and the chaotic sea arise from the two shortest periodic orbits (po's) of the corresponding configuration δ (see Fig. 5). This is due to the fact that for every eccentric configuration with $r > \delta$, the first—i.e., the shorter—po is hyperbolically unstable (upo) and the second—i.e., the longer—po is elliptically stable (spo). Thus both together yield the typical structure of the phase-space sections. In the concentric case $\delta = 0$, both orbits coalesce—i.e., have the same length—and show neutrally

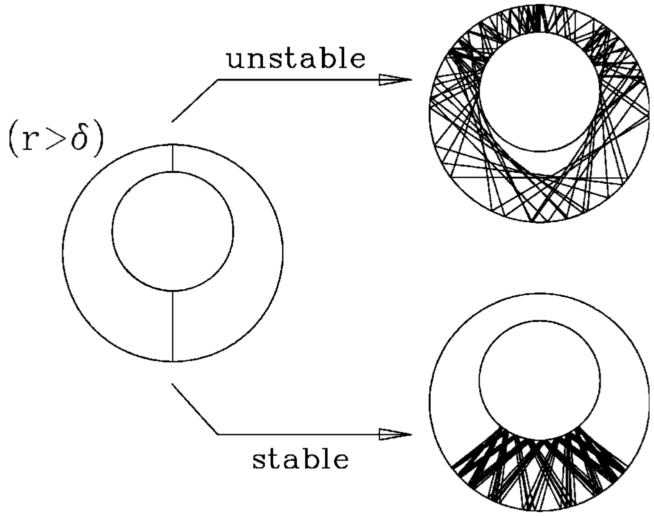

FIG. 5. Universal stability behavior for the shortest periodic orbits in case of $r > \delta$. For details see Sec. II B.

stable—i.e., bouncing ball—characteristics (bbo). As soon as the system becomes slightly eccentric, both orbits are separated according to the Kolmogoroff-Arnold-Moser (KAM) or Poincaré-Birkhoff scenario [39–41]. They provide one stable and one unstable fixed point, which show the characteristic phase-space structures under perturbation. The same occurs successively for every originally neutrally stable fixed point: namely, every periodic orbit of the concentric systems.

The only neutrally stable po's that persist for any $\delta \neq 0$ are located within the whispering gallery region. Two orbits of this type (with positive and negative sense of motion) are given in Fig. 4 for the cases of $\delta = 0.05$ and 0.20. There is no dependence on the eccentricity, since the orbits shown do not hit the inner circle for the considered values of δ. As described above, the conservation of angular momentum manifests itself by invariant horizontal lines in the *LS* plane. The clearly visible separatrix in Fig. 4 at $\delta = 0.05$ plays a particular role for the topological structure of the phase space. It separates two types of orbits from each other: those ones, which are mapped onto themselves under a reversal of the sense of motion (i.e., a reflection with respect to the axis $S = 0$), and orbits, which are mapped onto the opposite side of the phase space. In addition the latter ones feature a transition from starlike to whispering-gallery characteristics at $S = 0.75$ yielding the separation of chaotic and regular regions with increasing δ.

With increasing δ the chaotic sea fills the gap between the two separated whispering gallery regions. In classical mechanics, a transition between cw and ccw whispering gallery trajectories is *not* possible. The Poincaré surfaces of section show such a transition for trajectories just below the two borders of the whispering gallery regions ($|S| \lessapprox 0.75$): The ergodic features of transport within the chaotic sea become more and more effective with increasing δ. This is confirmed by calculations of the classical rate of transport as a function of δ [16]. According to this calculation, there is an effective coupling between phase-space regions in the direct vicinity of the two whispering gallery strips. The coupling can be strongly enhanced by increasing the size of the chaotic sea.

We have characterized the structure of the classical phase space and thereby provided the information necessary for an understanding of the properties of the quantum counterpart. The following sections deal with the corresponding quantum annular billiard and its experimental investigation. They show that the classically separated whispering gallery regions are coupled by the mechanism of chaos-assisted tunneling.

III. CONCENTRIC QUANTUM ANNULAR BILLIARD

In order to characterize the observables relevant for tunneling, the present section considers the concentric quantum annular billiard of the family $r + \delta = 0.75$. Its eigenstates result from the quantization of the whispering gallery tori. Very much as the classical whispering gallery trajectories, these quantum whispering gallery states occur in pairs, so-called doublets.

Due to rotational symmetry, the annular billiard with $\delta = 0.0$ is integrable. Not only the energy $\mathcal{E}$, but also the angular momentum $\vec{\mathcal{L}}$ is a constant of motion. The quantum system is described by the stationary Schrödinger equation

$$(\Delta + k^2)\Psi(\vec{r})|_{\mathcal{G}} = 0 \tag{3}$$

inside the billiard's domain $\mathcal{G}$, with Dirichlet boundary conditions

$$\Psi(\vec{r})|_{\partial\mathcal{G}} = 0. \tag{4}$$

The eigenvalues of this regular billiard can be calculated by the transcendental equation

$$J_n(k_{n,m}r)Y_n(k_{n,m}R) - J_n(k_{n,m}R)Y_n(k_{n,m}r) \overset{!}{=} 0. \tag{5}$$

Due to the integrability, the quantum states are well defined by two quantum numbers: The angular momentum quantum number $n = 0, 1, \ldots$ and the radial quantum number $m = 1, 2, \ldots$. The functions J_n and Y_n are the Bessel and Neumann functions of the first kind and nth order. Using polar coordinates, the eigenfunctions have the form [16,42]

$$\Psi_{n,m}(\rho,\varphi) = \mathcal{A}_{n,m}[J_n(k_{n,m}\rho)Y_n(k_{n,m}R) - J_n(k_{n,m}R)Y_n(k_{n,m}\rho)] \times \begin{cases} \cos(n\varphi), \\ \sin(n\varphi). \end{cases} \tag{6}$$

They are normalized to unity via $\mathcal{A}_{n=0,m} = k_{n=0,m}\sqrt{\pi}/2$ and $\mathcal{A}_{n\neq 0,m} = k_{n\neq 0,m}\sqrt{\pi/2}$. This defines two types of states: The first set with $n = 0$ consists of singlets possessing rotational symmetry; the second set with $n \neq 0$ consists of twofold-degenerate states—i.e., doublets—without any rotationally symmetric structure (see Fig. 6).

Obviously, this quantum feature reflects the structure of classical phase space. Only those types of trajectories with classical angular momentum $S \neq 0$ are arranged in pairs with different senses of motion (see Sec. II). An Einstein-Brillouin-Keller (EBK)- or Bohr-Sommerfeld quantization of Eq. (2),

$$\mathcal{L} = |\vec{\mathcal{R}}||\vec{\mathcal{P}}|\sin\alpha = \hbar k S \overset{!}{=} n\hbar, \tag{7}$$

yields

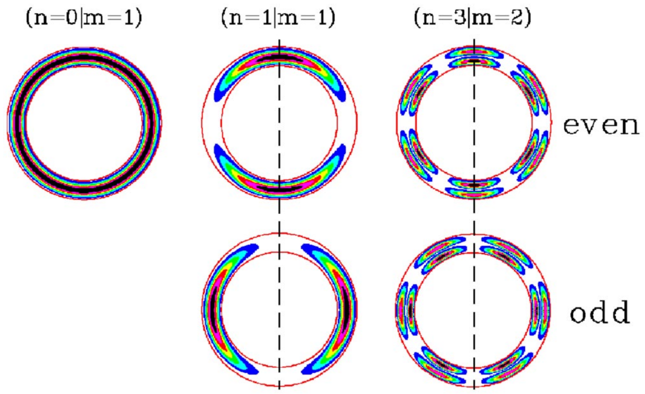

FIG. 6. (Color online) Squared wave functions of the concentric system with $r=0.75$ according to Eq. (6). On the left side the first singlet (with rotational symmetry) is given; the middle part shows the first doublet (with even and odd parity, respectively). The right-hand part shows a higher excited doublet for better understanding of the quantum numbers (n,m).

$$S=\frac{n}{k}. \tag{8}$$

From this, the classical angular momentum S which is assigned to a given quantum doublet can be identified in the corresponding phase-space portrait.

It is instructive to see how the classical property "sense of motion" (the sign of S) is translated into the quantum picture. The two states of a doublet may be distinguished from each other by their parity with respect to the billiard's (arbitrarily chosen) line of symmetry (see the vertical dashed line in Fig. 6). Obviously, this line is well defined after transition to eccentric configurations of the billiard. Both features—the classical sense of motion as well as the quantum property of parity—are directly related to the reflection symmetry of the system.

After calculating from Eq. (5) an eigenvalue for a given angular momentum quantum number, the position of the corresponding quantum state within the classical phase space can be determined with the help of Eq. (8). In Fig. 7, this is displayed for the spectrum of the concentric configuration with $r=0.75$. For later comparison with the microwave experiments described in the next section, the conversion from eigenvalues to eigenfrequencies has already been carried out. This is achieved by $f=c_0k/2\pi$ if the radius R of the outer circle is converted from theoretical dimensionless units—i.e., $R=1$, to $R=1/8$ m$=125$ mm. The spectrum has been calculated within the frequency range up to 20 GHz. Figure 7 shows a branch for each radial quantum number m. Each branch starts on the abscissa with the angular momentum quantum number $n=0$, which denotes a rotationally symmetric singlet. The eigenfrequency is a monotonic function of the angular momentum S. For better orientation, the borderline of the chaotic sea at $S=0.75$ is given in the figure. In addition, the positions of three selected doublets with quantum numbers $(n=10|m=1)$, $(20|1)$, and $(30|1)$ are marked on the first branch. Besides their eigenfrequency they significantly differ in their quantized angular momentum S.

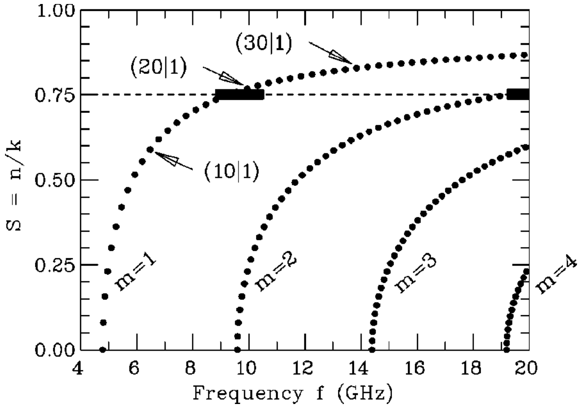

FIG. 7. Eigenfrequencies vs quantized angular momenta according to Eq. (8) for the concentric system with $r=0.75$. The dashed line at $S=0.75$ marks the borderline (the "beach") between the chaotic sea and the whispering gallery region in the classical phase space of the present setup. The solid bars denote those important spectral regions, where quantum states pass the borderline and thus couple the otherwise distinct phase-space regions.

Within the picture of coupled but classically distinct phase space regions, Fig. 7 may be used as a map for the observation of chaos-assisted tunneling. The three displayed doublets should exhibit a characteristic motion when the eccentricity is changed from the concentric geometry $(\delta=0)$ towards an eccentric configuration $(\delta\neq 0)$ (see Fig. 4). Doublets with high angular momentum [such as, e.g., $(30|1)$] are located within the whispering gallery region, and thus an increase in δ should not change them; i.e., the eigenfrequency should not move and the splitting should remain extremely small. The higher the angular momentum quantum number of a quasidoublet, the easier to find it in the spectrum of an eccentric case, since the position shows an even weaker change with variations of δ.

Following steadily the branch with $m=1$ towards smaller angular momenta, the whispering gallery region is gradually left until the coupling to the chaotic sea becomes optimal at $S=0.75$. Exactly here, the doublet $(20|1)$ is located. For the eccentric configurations, where angular momentum is not a good quantum number anymore, it comes to an enhanced "smearing of states in angular momentum space" at this borderline (broad Fourier spectrum in S); i.e., from the quantum point of view an overlap between whispering gallery region and chaotic sea is realized. In this case, the classically forbidden tunneling between whispering gallery trajectories with opposite senses of motion shows a maximum strength. The quantum spectrum is expected to display a corresponding maximum splitting of quasidoublets in the vicinity of this borderline—i.e., "on the beach" of the chaotic sea [17–20]. Therefore these beach modes play a particular role in the experimental observation of dynamical tunneling. As can be seen from Fig. 7, there exist only two windows at 8.75–10.50 GHz and at 19.25–20.00 GHz, which are accessible in the present experiment (solid bars).

We have so far characterized the concentric quantum annular billiard. This could be done with analytic calculations, as the system is integrable. For a detailed investigation of the chaos-assisted tunneling, however, one has to study the ec-

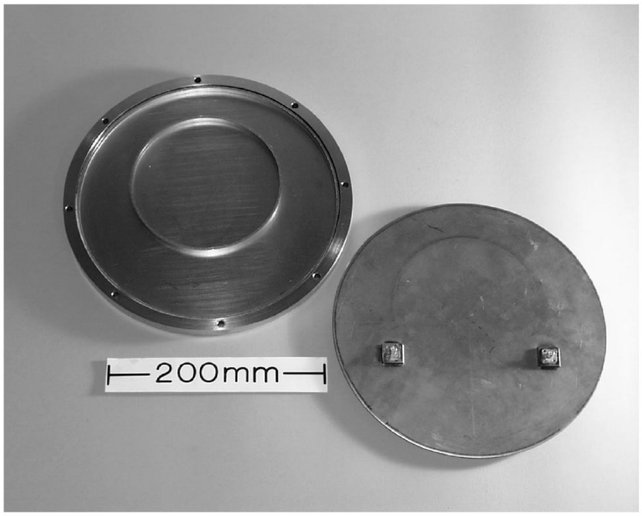

FIG. 8. Modular microwave resonator of the niobium annular billiard with an outer circle of radius $R=125$ mm. The lid on the right-hand side has two antennas for the excitation of the electromagnetic fields.

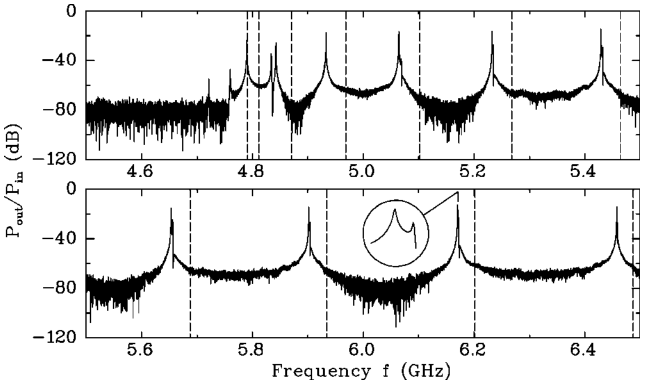

FIG. 9. Excerpt from the transmission spectrum of the superconducting resonator in the concentric configuration $\delta=0.0$. The dashed lines mark the theoretical positions of the eigenvalues calculated from Eq. (5) for all the states from $(0|1)$ to $(10|1)$.

centric cases. These are not accessible analytically, although the whispering gallery modes can to some extent be approximated by eigenfunctions of the concentric system. In the following sections we describe in detail the investigation of the annular billiard with the eccentricities $\delta=0.05$, 0.10, 0.15, and 0.20 (see Fig. 4) with the help of microwave experiments.

IV. MICROWAVE EXPERIMENTS

In what follows we discuss the methods of experimental verification of the above scenario. This includes the details of the identification of quasidoublets. The measurements consist of two separated experiments: First, spectra of a superconducting niobium billiard ($T=4.2$ K) were measured, allowing the observation of quasidoublets. Second, the experimental mapping of relevant wave functions (intensity distributions) has been performed on a geometrically identical copper resonator ($T=300$ K) in order to assign the angular momentum.

A. Measurements using the superconducting resonator

The superconducting resonator was constructed from modular niobium parts (with the critical temperature $T_c=9.2$ K). The resonator has the height $h=7$ mm and is closed by a lid equipped with two antennas, as can be seen in Fig. 8. From the spatial dimensions results the transition frequency $f_t=c_0/2/h\approx 21.4$ GHz. Below this frequency, the billiard behaves fully two dimensional, and therefore, the electromagnetic resonator represents a system which is analogous to the quantum billiard. An overview of this technique, our typical experimental setup, and selected experiments can be found in [34,43]. The inner circles were all manufactured as freely movable rings of the desired radii. From this "construction kit" several configurations (r,δ) of the annular billiard can be realized. To obtain a good electric contact between the different parts, we used commercially available solder wire of 1.2 mm in diameter. This wire was mounted in a groove located on outer rims of the components. The closed billiard was tightly bolted together using a robust casing of stainless steel.

Besides geometrical imperfections of the resonator—e.g., inexact positioning or manufacturing tolerances of individual parts—the real and ideal annular billiards differ by the microwave antennas used for excitation. To estimate their perturbing influence on the symmetry of the system and therefore on the positions and especially on the splittings of quasidoublets, we used *two different* resonator lids with essentially different antenna positions in our measurements. In case of the first setup (lid A), the antennas were located at $S=0.907$, expressed in units of the angular momentum—i.e., within the whispering gallery region—so that larger perturbations of the relevant quasidoublets above $S=0.75$ were expected. In case of the second lid (B), the antennas were moved to the position $S=0.625$ far below the border line with $S=0.75$, so to speak inside the shadow region of the inner circle. Due to these geometrically different antenna patterns, lid B allowed us to investigate the configurations $\delta=0.10$, 0.15, and 0.20, whereas lid A allowed us to measure the cases $\delta=0.0$ and 0.05.

In all eight measurements, the microwave spectrum was recorded in the range up to 20 GHz with a resolution of 10 kHz. During the measurements, which typically took 13–15 h for each configuration, the billiard was mounted inside an evacuated copper box, which itself was immersed in liquid helium. In equilibrium, the billiard remained at a temperature of 4.2 K and a pressure of approximately 2 mbar.

Figure 9 shows a part of the spectrum for the concentric configuration $\delta=0.0$ in transmission mode. The power transmitted to antenna 2, P_{out}, is measured with respect to the power put into antenna 1, P_{in}, as a function of frequency. The theoretical eigenvalues for the states between $(0|1)$ and $(10|1)$, expected according to Eq. (5), are marked with dashed lines in the figure. One clearly sees that the experimental resonances fall in general slightly below the calcu-

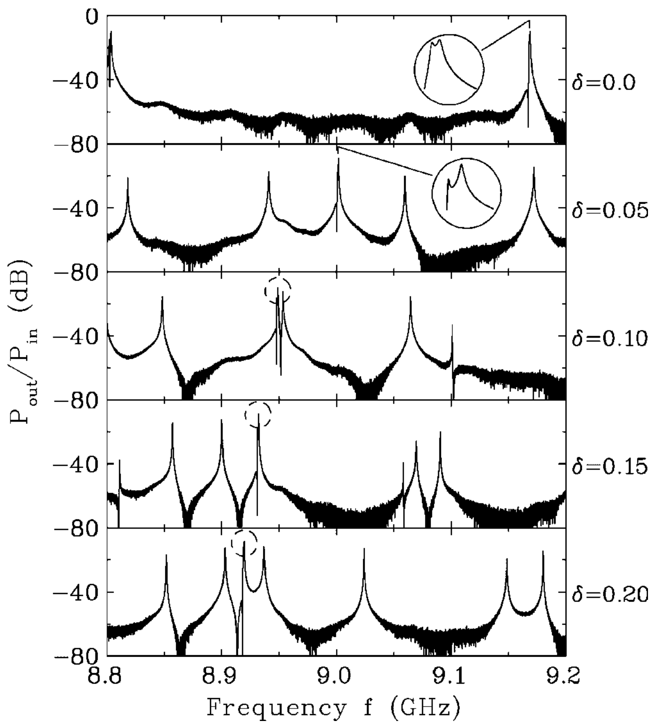

FIG. 10. Excerpt from the transmission spectrum for the superconducting resonator (lid A) as a function of the eccentricity δ. Besides a large number of singlets exactly one quasidoublet is observed. The circles mark and enlarge this doublet. They show a systematic motion towards smaller frequencies with increasing δ. The frequency axis has been stretched by the factor of 10 in the magnifications.

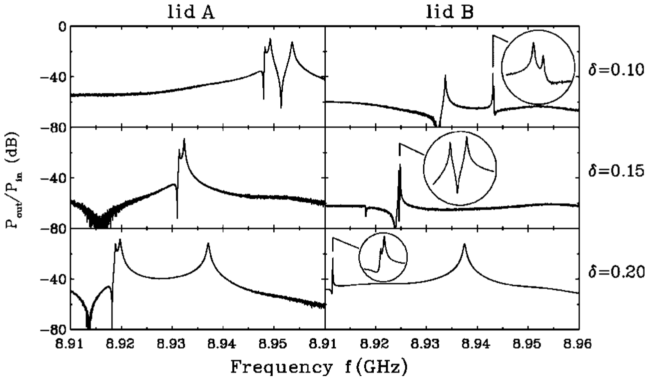

FIG. 11. The quasidoublet taken from Fig. 10, measured with strongly (lid A) and weakly (lid B) perturbing antennas. The frequency axis is stretched by the factor of 10 in the magnifying circles.

lated values, in spite of the thermal contraction of the resonator. Furthermore, the first modes with a low-angular-momentum quantum number n show a strong splitting of the doublets. Both effects systematically decrease for higher n. This is due to imperfections of the mechanical setup and of the adjustment of the resonator components. On the other hand, the antennas which were used for excitation (here lid A was installed) lead to an observable splitting for high n. Especially in the case of higher angular momenta the exact position and shape of the inner circle become less and less important: The perturbation saturates in the position of a given doublet as well as in the magnitude of its splitting. In context with the measurements of field distributions, we shall reconsider this in more detail.

An excerpt from the frequency window between 8.75 and 10.50 GHz is given in Fig. 10. It will be important for the subsequent analysis. Here, the transmission spectra for the configurations $\delta=0.0$, 0.05, 0.10, 0.15, and 0.20 are displayed. They have been taken with the antennas of lid A. A closer look reveals, besides a large number of singlets, *exactly one* quasidoublet (marked by a circle). It shows a decreasing shift with increasing eccentricity and eventually reaches an almost fixed position in the spectrum. This is in perfect agreement with theoretical predictions [44]. As mentioned above, even the concentric case $\delta=0.0$ displays a measurable splitting. This is due to strongly perturbing antennas within the whispering gallery region (lid A). To estimate such an influence for the case of eccentric configurations, we used lid B with only slightly perturbing antennas outside the whispering gallery region. Since in this case the antennas were located inside the shadow region of the inner circle, only the eccentricities $\delta=0.10$, 0.15, and 0.20 were accessible. For these configurations, Fig. 11 enlarges the quasidoublet of Fig. 10 in a direct comparison. For lid A, the splitting as well as the shape of the double resonance shows nearly no dependence on the eccentricity. With lid B the measurements display strong fluctuations: Besides a strong decrease of the splitting, the figure reveals for the first time in our investigation a significant dependence on the chaoticity. Fluctuations of the quasidoublet splitting as a signature for an interaction with the chaotic singlets are theoretically expected, especially in the vicinity of crossings [14,16].

Hence, the experimental observation of chaos-assisted tunneling will be essentially based on measurements with lid B. The series of measurements with lid A and the mapping of billiard wave functions, described in the next subsection, are used to well identify the quasidoublets, to determine the associated (approximate) quantum numbers $(n|m)$, and to deduce the corresponding position in phase space—i.e., the quantized angular momentum S. Since Eq. (8) was originally derived for the regular, concentric case with conserved angular momentum, it is only approximately correct in the eccentric scenario. However, also in the case of $\delta\neq 0$, quasidoublets show positions and splittings, which systematically approach the exact doublets of the concentric case when angular momentum and energy increase.

B. Measurements using the normal conducting resonator

For a proper identification of quasidoublets a second experimental setup was developed in order to measure electromagnetic intensity distributions, which correspond to quantum probability densities. The structure of whispering gallery states would easily allow us to assign the corresponding quantum numbers, so that the determination of the quasidoublet's position in the classical phase space becomes possible. Therefore, besides the energy $\mathcal{E}$, the quantized angular momentum S may be systematically deduced as a function of the eccentricity δ. In this way its relevance for chaos-assisted tunneling would be proven.

The experimental setup consists of a normal conducting copper resonator, which was manufactured as a copy of the superconducting billiard. As in the case of the niobium "twin," the copper resonator was composed modular components. In contrast to the niobium resonator, which at 4.2 K is not accessible for geometrical manipulations, room temperature (300 K) allows us to map wave functions by means of a field perturbation method originally introduced in accelerator physics [45]. For a couple of years, this method was not only used in the framework of quantum chaos [46–49], but as well to observe pure electromagnetic field distributions in a three-dimensional (3D) Sinai billiard [50].

The principle of these measurements relies on the fact that the standing electromagnetic wave inside the cavity is perturbed by a small body. In this way, the integrated ratio of stored electric and magnetic energy changes. As a consequence, the resonator exhibits a slight shift of its resonant frequency f_0. Formally, a small metallic body yields

$$\partial f(\vec{r}) = f_0 - f(\vec{r}) = f_0(c_1\vec{E}^2(\vec{r}) - c_2\vec{B}^2(\vec{r})), \qquad (9)$$

where the constants c_1 and c_2 are determined by its size and shape. Accordingly, the electric term in Eq. (9) may drastically differ from the magnetic term.

The task was then to adequately choose a perturbing body (including its positioning unit) such that the body could be moved inside the resonator. Furthermore, mainly the electric component of the field should be affected (the B term should be suppressed), since only in this case the correspondence with the quantum wave function is given. For the present experiments, a magnetic coupling between the perturbing body and the positioning unit provides a very elegant solution as it was shown in other microwave experiments [46–48]. The perturbing body itself consists of a Ferrit-based permanent magnet with linear dimensions of ≈1 mm. It was held tight and positioned through the billiard's bottom plate (5 mm of copper) by help of an axially premagnetized guiding magnet with diameter of 3 mm. The guiding magnet itself was mounted on a special positioning unit, consisting of two PC-controlled step motors. This concept allows to move the body on a polar coordinate grid with practically arbitrary (motor-restricted) resolution.

Figure 12 shows the experimental setup. This device allows us to measure any desired electromagnetic field distribution of the annular billiard with parameters r and δ with high geometrical resolution. We typically used 1/10 of the wavelength. Besides the positioning of the perturbing body, a PC simultaneously controls a network analyzer, determining frequency shifts $\partial f(\rho,\varphi)$ via very sensitive phase measurements (see also Fig. 13). According to Eq. (9) this finally yields the local electromagnetic field intensity.

Since the material of the perturbing bodies is given by our positioning method, only its geometrical shape could be adjusted to the desired suppression of the $\vec{B}$ component in Eq. (9). In the quasi-two-dimensional resonator (with a transition frequency $f_t \approx 30$ GHz, resulting from its height of 5 mm) the electric field vector is perpendicular to the bottom of the billiard and the magnetic field vector is parallel to its plane (TM_0 modes): These facts are used for an effective separation of both components of the electromagnetic field. As described in [45], the interaction with a metallic body becomes optimal for an orientation along the lines of the electric field. Therefore, we used metallic cylinders oriented perpendicularly to the billiard plane. With growing length and shrinking cross section such cylinders show more and more the desired electric component, while the $\vec{B}$ component is affected less and less. With increasing ratio length/radius of the body, the measured field distribution becomes more and more proportional to the exact quantum wave function $|\Psi|^2$.

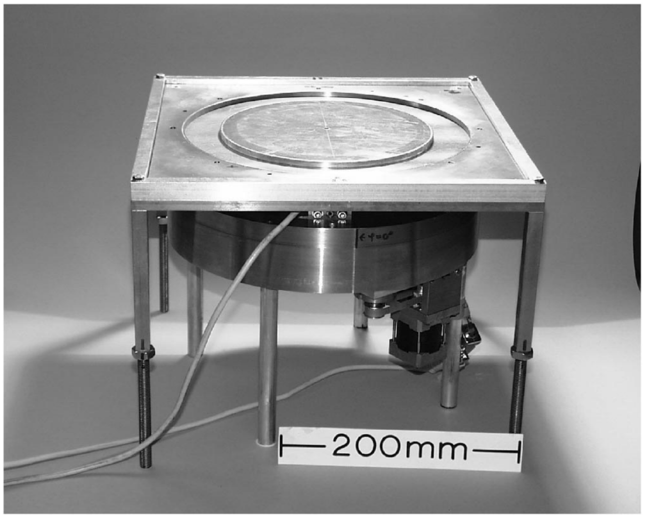

FIG. 12. Photograph of the experimental setup, which was used to measure electromagnetic intensity distributions. At the top, the open billiard in concentric configuration is seen. Below this, the positioning unit for the perturbing magnetic body, properly aligned to the resonator, is shown. The guiding magnet is located directly below the bottom plate of the billiard on a movable sledge, which is positioned by two stepper motors.

A cylindrical body with the length of 1.84 mm and the diameter of 1.00 mm (this yields a volume of 1.45 mm^3)

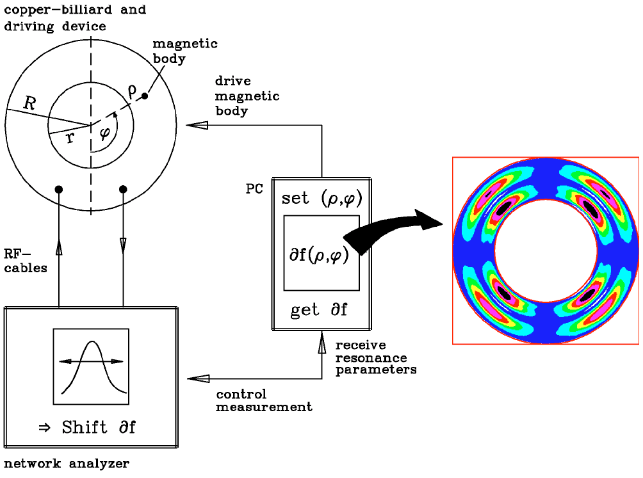

FIG. 13. (Color online) Principle of control of the experimental mapping of electromagnetic field distributions in the annular billiard. The PC sets the position of the perturbing body and sends commands to the network analyzer. The measured frequency shift ∂f is recorded as a function of the position (ρ,φ).

turned out to be the best choice. The resolution of ten sampling points per wavelength requires a two-dimensional grid with 200 (at 2 GHz) to 20 000 (at 20 GHz) points. The above perturbing body ensured a safe and accurate guidance with maximum errors in the range of $1-2$ mm in the absolute position. This guarantees the spatial resolution even at 20 GHz and the errors lie in the range of the general adjustment tolerance for the positioning unit (not exceeding 1 mm). In repeated measurements performed under identical conditions the frequency shifts could be reproduced within 5%.

C. Measurement of the family $r+\delta=0.75$

Before the measurements are described in detail, some estimates of the resolution and errors shall be given. We discuss to which extent experimental verification of the theoretical predictions depends on the interplay between the 4-K and 300-K setups. In particular, we have to specify the ranges of resolution, which are accessible by the two test stands, and the resolution which is necessary to allow the observation of chaos-assisted tunneling.

As shown in [16], for an unambiguous verification of chaos-assisted tunneling, relative quasidoublet splittings $|\Delta f/f|$ have to be followed over about 18 orders of magnitude as a function of the eccentricity δ. However, even for superconducting resonators, a maximum resolution of the order of the reciprocal quality factor, $1/Q\approx10^{-6}$, may be expected. Nevertheless, as shown in [17–20], there exists a very special class of quasidoublets, for which experimental observation of their splitting seems to be realistic. This class of so-called beach modes is characterized by an angular momentum that locates them directly on the borderline of the chaotic sea in the classical phase space. This provides an optimal coupling between the whispering gallery region and chaotic states. As a consequence, the quasidoublet splitting is amplified by several orders of magnitude at $S=0.75$.

For a demonstration, Fig. 14 displays the theoretically expected splittings within this important window [51] for three experimentally investigated configurations (δ=0.10, 0.15, and 0.20). The figure shows the quasidoublet splittings of the family with the radial quantum number $m=1$ in the range of $n=10-30$ as a function of the quantized angular momentum $S=n/k$. The border of the chaotic sea splits the figure into two parts: Below the beach—i.e., inside the classically chaotic region—larger splittings are correlated with larger eccentricities—i.e., chaoticities—of the billiard. In contrast, beyond the borderline, the quasidoublets display strong fluctuations accompanied by decreasing splittings (on the average) for increasing angular momenta in this regular phase-space region. The fluctuations are caused by crossings between quasidoublets and adjacent chaotic states [14,16]. The most striking "indication" of chaos-assisted tunneling is just given by this emerging *maximum structure* in the distribution of splittings directly on the beach at $S=0.75$.

The usage of a superconducting resonator should indeed allow us to observe this effect of chaos-assisted tunneling above the resolution limit ($|\Delta f/f|=10^{-6}$). Beach modes are expected to fall right inside the frequency windows between 8.75 and 10.50 GHz and between 19.25 and 20.00 GHz, respectively (see also Fig. 7). In order to detect their particular splitting, we included further windows with quasidoublets inside the chaotic sea [mode $(10|1)$] as well as inside the whispering gallery region [modes $(27|1)$–$(30|1)$] in our experimental investigation. These additional quasidoublets lie on the borders of the region shown in Fig. 14. This extension of the experimentally investigated range is only possible with the high resolution of the superconducting resonators as well as the unambiguous identification of the quantum numbers in the maps of the wave functions. Since the normal conducting resonator promises quality factors only in the range of $Q\approx10^{3}-10^{4}$, we briefly discuss the spectral properties of our geometry, in order to estimate its experimental limits.

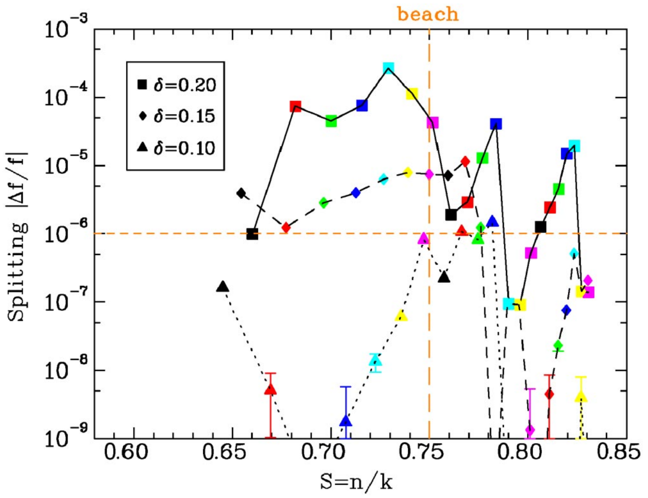

FIG. 14. (Color online) Theoretically predicted quasidoublet splittings in the vicinity of the beach of the chaotic sea at $S=0.75$ (dashed vertical line) as a function of the quantized angular momentum $S=n/k$. The calculated data points for three of the investigated billiard configurations (δ=0.10, 0.15, and 0.20) are marked by different symbols and are interconnected. In addition, all the different quasidoublets $(10|1)$–$(30|1)$ are sorted by grey scales. Here, related data points of a given state $(n|1)$ fall one upon the other and are denoted by one grey scale level. The dashed horizontal line at $|\Delta f/f|=10^{-6}$ shows the experimental limit of resolution.

Table I gives for all configurations of the annular billiard the expected mean values for the number of levels, N^{smooth}, according to the Weyl formula [52], the level density ρ^{smooth}, the level distance D, and the resulting minimum quality factor Q_{min}, which is necessary to resolve levels at 10 and 20 GHz, respectively. The respective minimum quality factor for resolving two levels increases continuously with the eccentricity δ (factor of $\lesssim2$) and even stronger with the frequency f (factor of $\gtrsim4$). Especially for high δ and high f resolving resonances with the normal conducting resonator becomes more and more difficult. Nevertheless, especially in the relevant window around 10 GHz the copper billiard will allow us to distinguish resonances separated by the corresponding mean level spacing D as long as the antennas provide sufficient coupling to a given field distribution. On the other hand, a comparison with the splittings of Fig. 14 clearly rules out a direct verification by using the normal

TABLE I. Basical spectral properties of the investigated annular billiards at a frequency of 20 GHz [10 GHz].

Configuration	$\delta=0.0$	0.05	0.10	0.15	0.20
N^{smooth}	255	306	353	398	438
	[52]	[65]	[78]	[89]	[99]
ρ^{smooth} (GHz^{-1})	28	33	37	42	46
	[13]	[15]	[18]	[20]	[22]
D (MHz)	36	30	27	24	22
	[79]	[65]	[57]	[50]	[46]
Q_{min}	555	656	750	837	917
	[127]	[153]	[177]	[199]	[219]

conducting setup only, even if only the largest splittings are considered. This means that the copper billiard will not allow us to resolve both modes of a given quasidoublet and that slight splittings of doublets can only be resolved with a superconducting resonator (as in [53]).

Figure 15 shows the measured transmission spectrum in the frequency range between 8.88 and 8.96 GHz, obtained with the copper billiard at 300 K and with the niobium resonator at 4.2 K, respectively, both of them using lid *A* in the configuration $\delta=0.20$. Above these spectra, the field distributions, as measured via resonances of the normal conducting setup, are presented. This demonstrates how the resonances, emerging from the 4-K measurements (see Figs. 10 and 11) could be successively identified in a systematic way. The assignments between the results for the warm and cold resonators are obvious. As described in Sec. IV A, the displacements of resonances between the two measurements, which based on practically identical billiards, are due to imperfections of the geometry and perturbations of the system's symmetry. Obviously, at least in the window around 10 GHz these displacements are smaller than the mean level spacing and therefore tolerable. In addition, Fig. 15 nicely allows us to verify the above-mentioned properties: The state in the middle is clearly the beach mode with quantum numbers $(n=18|m=1)$, indicating a typical field structure as expected also for higher-lying whispering gallery states. Indeed, the measurement at 300 K shows only one broad resonance and just that field distribution, which is excited more effectively. Only in the 4-K measurement the quasidoublet structure with both states of different parity is clearly visible. All other modes possess a chaotic structure with strong field contributions from outside the whispering gallery region. Consequently, these modes emerge as singlets in the spectrum of the superconducting resonator.

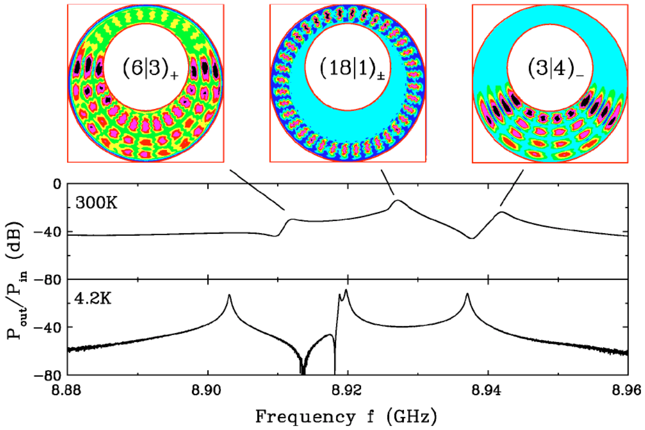

FIG. 15. (Color online) Comparison between the normal conducting (300 K) and the superconducting (4.2 K) measurement and identification via experimentally obtained field distributions [quantum numbers $(n|m)$ including parity] for the configuration $\delta=0.20$.

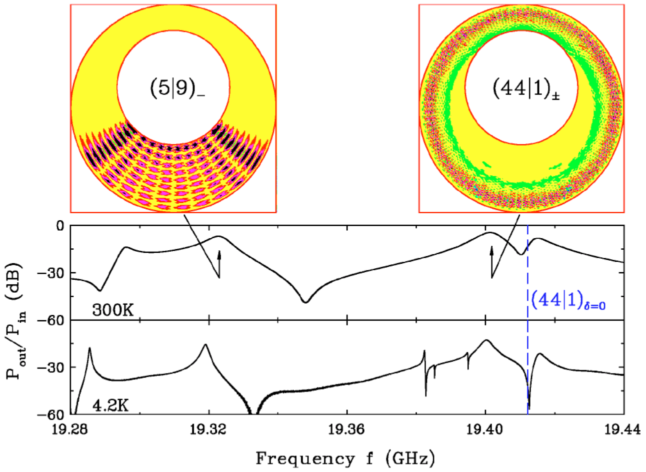

FIG. 16. (Color online) Comparison between the warm and the cold measurements at very high frequencies. For notation see Fig. 15. The position of the whispering gallery mode $(44|1)$ is nearly invariant under variations in δ (dashed line for $\delta=0$).

Figure 16 demonstrates that the field distribution measurements apply without any problem even at frequencies around 20 GHz. Again, spectra of the configuration $\delta=0.20$ at 300 K and 4.2 K using lid *A* are shown, this time in the range between 19.28 and 19.44 GHz. Among a large number of chaotic states, the very highly excited whispering gallery mode $(44|1)$ could be found and has been clearly identified using again a local resolution of $1/10$ of the given wavelength. The expected position of the corresponding concentric eigenfrequency ($\delta=0.0$, dashed line) confirms that whispering gallery modes with increasing excitation energy show a smaller and smaller displacement in their frequency, even if the eccentricity is far away from the concentric case (here $\delta=0.20$). The figure shows that a principle assignment of both spectra at 300 K and 4.2 K, respectively, is still possible. Due to the high level density, however, it becomes impossible to resolve very closely lying modes in the normal conducting billiard and to assign these modes to resonances of the superconducting resonator. Therefore the following analysis will mainly concentrate on the frequency range around 10 GHz and only a few quasidoublets between 12 and 14 GHz will be considered.

In order to include not only the quasidoublets, which are relevant for chaos-assisted tunneling, in the analysis but also chaotic states, all measured field distributions will be systematically classified by two quantum numbers. This procedure accounts for the fact that every state of an eccentric configuration is nothing but a δ-variation-induced geometrical defor-

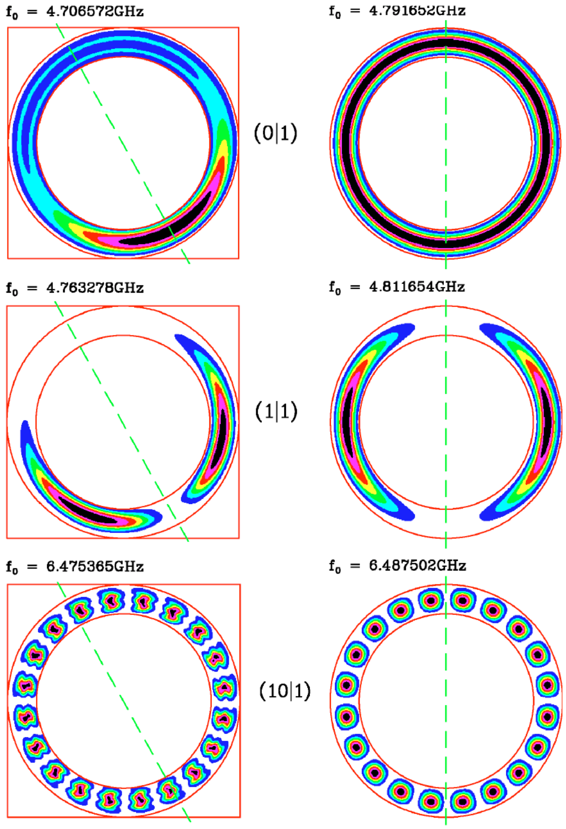

FIG. 17. (Color online) Comparison between experimentally measured (left side) and numerically simulated (right side) states for different angular momentum quantum numbers n of the concentric system. Tiny perturbations of the eccentricity lead to the development of a tilted line of symmetry.

mation of a corresponding state in the concentric system. In this picture chaotic modes represent strongly deformed states, while whispering gallery modes represent weakly deformed states of the concentric billiard. The strength of this deformation simply reflects that a changing eccentricity has a considerably stronger impact on some states than on others due to their different composition of angular momentum Fourier components. The assigned quantum numbers $(n|m)$ therefore become systematically "better" with increasing angular momentum of the states. That is exactly what distinguishes whispering gallery modes from chaotic ones.

To obtain a more vivid description of this scheme, Fig. 17 compares some modes of the concentric configuration $(r=0.75, \delta=0.0)$, as they were measured in the experiment with those calculated from Eq. (6), respectively. From this, even for a very precisely assembled copper resonator tiny perturbations of the geometry are sufficient to obtain considerable deformations of the field distributions and hence a lowering of the resonance frequency. This emerges especially for modes with a low quantized angular momentum $S=n/k$. Follow-up measurements of the cavity's geometrical shape yielded a total displacement between the two centers of the inner and outer circles, respectively, of only 0.6 mm as the origin of the perturbed rotational symmetry. This corresponds to an eccentricity of $\delta=4.8\times 10^{-3}$. As indicated in the figure, this also leads to the constitution of a new line of reflectional symmetry, which is tilted with respect to the old one (defined by the antennas) by an angle of ≈29°. This lack of adjustment therefore falls right within the generally expected range of geometrical imperfections of the mechanical setup, and hence, it is in principle unavoidable. In addition, this observation is in total agreement with Fig. 9, where geometrical perturbations within the superconducting resonator of the same order resulted in shifts of the modes towards lower frequencies, especially in the case of low-angular-momentum quantum numbers n. These shifts showed a stronger saturation with increasing n. The reason is that for an increasing $S=n/k$ the perturbation of rotational symmetry has a decreasing impact on the states, as can be seen from mode (10|1) in Fig. 17. At such high angular momenta, the perturbing influence of the antennas is again stronger than the symmetry breaking induced by the geometry itself. According to this, it is not possible to assign a proper parity to the experimental mode (10|1) with respect to the new line of symmetry as induced by the perturbation. In fact, once again the axis of the unperturbed system is preferred, since with respect to this line of symmetry the antennas are located symmetrically.

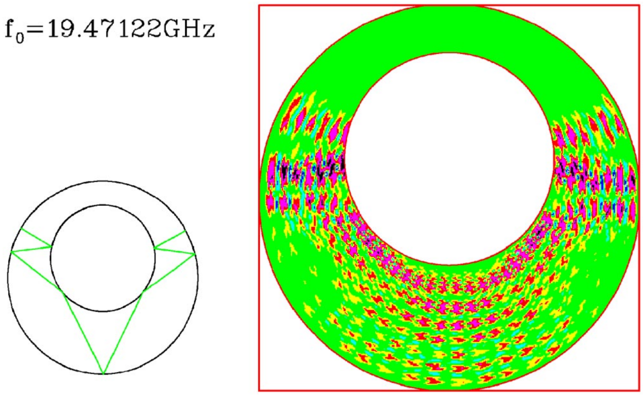

FIG. 18. (Color online) An example of a scar, found for the configuration $\delta=0.20$ in the frequency range around 20 GHz—i.e., at the upper end of the spectrum. On the left-hand side the corresponding unstable periodic orbit of the classical system is shown for comparison.

The figure also demonstrates how for an arbitrary deformation—i.e., for a certain eccentricity of the family $r+\delta=0.75$—even chaotic modes might be systematically labeled with the two quantum numbers (plus parity) of the originally unperturbed concentric modes, in just counting the number of half wave trains in the φ (giving $2n$) and ρ (giving m) directions, respectively. This has already been introduced in Figs. 15 and 16. In this way, nearly every measured field distribution has been characterized by two quantum numbers. The only exceptions are chaotic modes constituting a strong scar structure [54–56]—i.e., a strongly enhanced field amplitude along classically unstable periodic orbits. An example can be seen in Fig. 18. This assignment procedure between quantum numbers and field distributions was finally transferred to the resonances of the superconducting resonator. The results for the configurations with lid A, which also include the cases $\delta=0.0$ and 0.05, are given in the level schemes of Figs. 19 and 20. Here, the absolute positions of

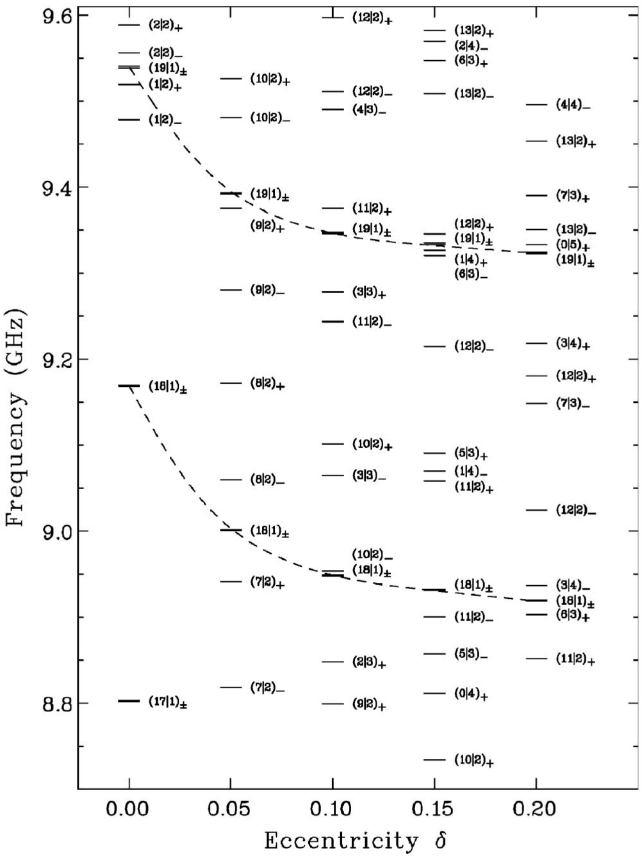

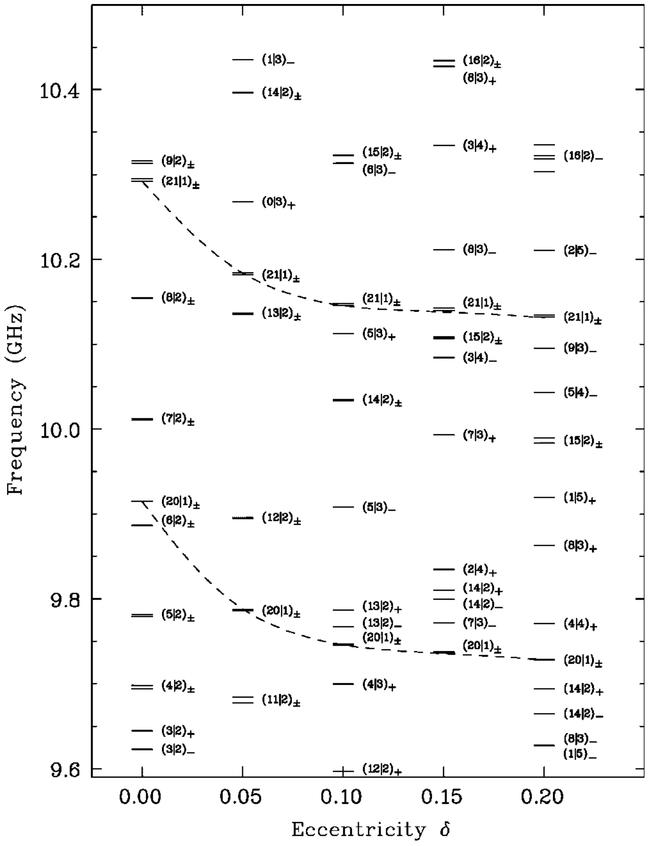

FIG. 19. Level scheme of identified resonances, experimentally taken using the superconducting resonator with lid A in the spectral range around 10 GHz. The dashed lines indicate the wandering of quasidoublets of the family $m=1$ as a function of δ.

FIG. 20. Sequel of Fig. 19.

the found resonances including the quantum numbers $(n|m)$ and parity are shown as a function of the eccentricity δ. Furthermore, the figure nicely demonstrates how in particular quasidoublets of the family $m=1$ move in the frequency spectrum under variations of δ (dashed lines). As stated above, this is a direct consequence of the deformation of the original concentric system under an increasing δ. Finally, every quasidoublet shows a saturation of this wandering at very high eccentricities, since the maximum possible extension of the field is reached, even if the size of the inner circle is further skrinked.

The higher the angular momentum S, the faster emerges the saturation and the smaller is the deformation of the concentric mode under variations in δ. To make this angular-momentum-dependent wandering effect more clear, Figs. 21 and 22 respectively, show mode $(10|1)$ (with $S\approx 0.59-0.66$) and the region around mode $(30|1)$ (with $S\approx 0.83$) in a direct comparison. Obviously, stronger frequency displacements as well as stronger changes in the field patterns can be observed for the modes with a lower-angular-momentum quantum number n.

In particular, the highly excited modes around $(30|1)$ will play a crucial role in the verification of chaos-assisted tunneling, since their large angular momentum guarantees a position far away from the chaotic sea. Their tiny quasidoublet splitting (see Fig. 14) should be even smaller than for the beach modes. This would finally prove that meaningful tunneling amplitudes can only be expected if the coupling between the whispering gallery region and the chaotic sea becomes more effective.

In a final step and for a quantitative investigation of this splitting behavior, all identified resonances of the normal conducting and the superconducting configurations were described by Lorentz curves. According to this, the exact eigenfrequencies f_μ as well as the widths Γ_μ [full width at half maximum (FWHM)] were determined with a relative accuracy of better than 5×10^{-7} in order to make use of the maximum accessible range of resolution (up to $Q\approx 10^6$) at the given spectral scanning using 10-kHz steps. Formally, this was achieved via a numerical fitting of the line shape

$$\left.\frac{P_{out}}{P_{in}}(f)\right|_{\text{linear}} = \sum_{\mu=1}^{N} \frac{C_\mu + D_\mu(f-f_\mu)}{(f-f_\mu)^2 + \frac{1}{4}\Gamma_\mu^2} + \sum_{\nu=0}^{G} B_\nu f^\nu \qquad (10)$$

to the data. This so-called "skewed Lorentzian shape" [57–59] is particularly suitable for the given set of data points. We note here, however, that recently an alternative description of resonances in microwave billiards has been derived [60]. Equation (10) allows the characterization of both isolated singlets ($N=1$) and strongly interacting quasidoublets ($N=2$). Here, C_μ and D_μ describe the strength of a certain resonance and the asymmetry of its line shape, respectively. In addition, these properties also characterize the

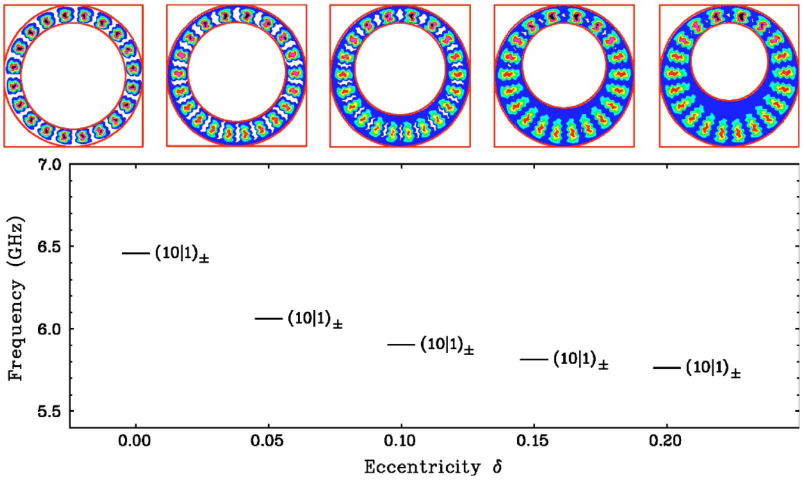

FIG. 21. (Color online) Mode $(10|1)$ under variations of the eccentricity δ. At the top the drastically changing field distributions can be seen, below the corresponding frequency shift.

influence of neighboring resonances. Furthermore, a more general background on the data is regarded by the second sum in Eq. (10). Taking small frequency windows, it is usually sufficient to reduce this expression to a straight line ($G=1$) for an adequate description of the data. For a demonstration of the quality of this procedure, which was performed with specific initial values and windows for each of the identified resonances, Fig. 23 shows the numerical fitting for the weakly excited quasidoublet $(29|1)_\pm$ of the configuration ($r=0.65, \delta=0.10$) in the superconducting state. These high-lying angular momentum states were excited so weakly that additional measurements with a resolution of 250 Hz instead of 10 kHz became necessary in the direct vicinity of the two resonances.

V. RESULTS

The starting point for the following analysis is given by the data sets as described in the previous section. To start with an overview, we will first give a summary of all those properties, which were involved in the investigation: the resonances of the geometrical configurations $\delta=0.0$, 0.05, 0.10, 0.15, and 0.20 for measurements at 300 and 4.2 K using strongly perturbing antennas (lid *A*) in the window 8.75–10.50 GHz (beach region) as well as mode $(10|1)$ (chaotic sea) and the modes $(27|1)$–$(30|1)$ (whispering gallery region). In addition, for the configurations $\delta=0.10$, 0.15, and 0.20 at 4.2 K using weakly perturbing antennas (lid *B*) all the states of the family $m=1$ between $(0|1)$ and $(30|1)$ were experimentally determined and included in the analysis.

For each individual resonance of the data set its position and its width were determined by means of Eq. (10) and finally labeled with its quantum numbers n (angular momentum), m (radial component), and p (parity). The crucial observable which allows an experimental access to chaos-assisted tunneling is basically the quasidoublet splitting of the whispering gallery states. Besides the dependence on the chaoticity of the system, we first will consider the question how the magnitude of the splitting is dominated by the corresponding position in phase space and whether a classification by chaotic, regular, and beach states can be confirmed in

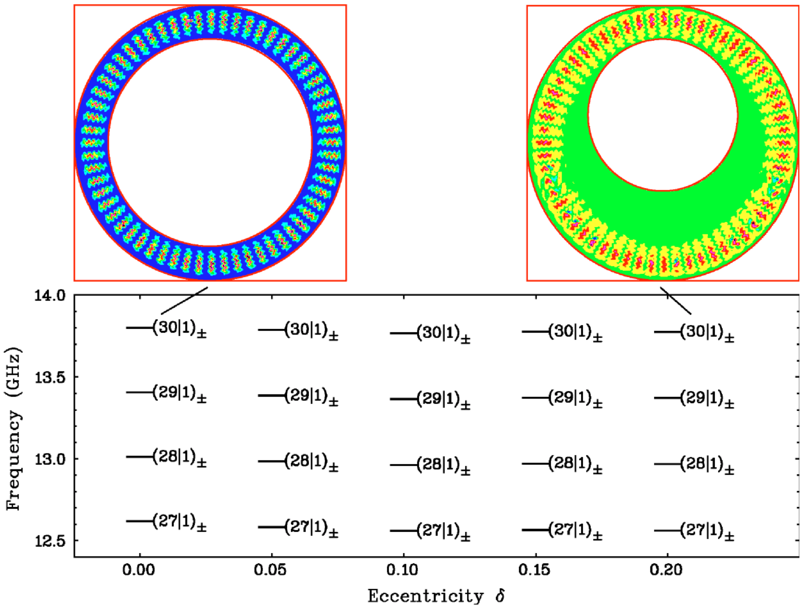

FIG. 22. (Color online) A spectral window for modes between $(27|1)$ and $(30|1)$, where the frequencies as well as the field distributions are nearly invariant under variations in δ.

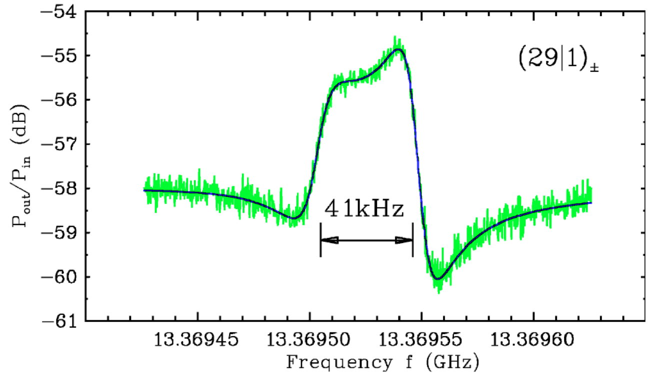

FIG. 23. (Color online) Numerical fit of the resonance shape given by Eq. (10) to the weakly excited quasidoublets $(29|1)_\pm$ of the configuration ($r=0.65$, $\delta=0.10$). In this case the resolution of the measurement was increased to 250 Hz, instead of 10 kHz. The relative splitting of the doublet is $|\Delta f/f| \approx 3\times 10^{-6}$.

the experiment. For this reason, Fig. 24 shows, for a *constant* eccentricity (here $\delta=0.20$), the normalized quasidoublet splitting $|\Delta f/f| \equiv |(f_{\rm even}-f_{\rm odd})/f_{\rm even}|$ versus the angular momentum $S=n/k$ with $k=(2\pi/c_0)(f_{\rm even}+f_{\rm odd})/2$. Here, every identified quasidoublet out of the window 8.75–10.50 GHz with quantum numbers n and m has been considered. The diagram displays the overall splitting behavior within a narrow frequency window—i.e., for a nearly constant energy—and allows a direct comparison of the three different experimental conditions. Due to a few insufficiently resolved resonances where the fit of Eq. (10) did not converge, the size of the data sets slightly varies. In all three subfigures the classification by chaotic and regular states becomes clearly visible. Low-angular-momentum quantum numbers n characterize states with strong contributions of the wave function outside the whispering gallery region and hence have to be denoted as chaotic. In contrast to this, modes with a high angular momentum are nearly exclusively localized right within the whispering gallery region and therefore are of regular nature.

The kind of illustration, which was chosen in Fig. 24, separates both types of states in a natural way by their by about three to four orders of magnitude differing splittings. Astonishingly, the radial quantum number m provides a sequential order of the states. Here, large radial quantum numbers ($m=3$–5) characterize chaotic states with a nearly constant splitting of the order of the mean level spacing or above (this depends on the number of m families in the present frequency window). Via the family with $m=2$ the quasidoublet splittings in the given frequency window experience the transition into the range of regular whispering gallery states with $m=1$. Strikingly, this transition is carried out in a very steady way and completed clearly before the classical borderline of the chaotic sea at $S=0.75$ is reached.

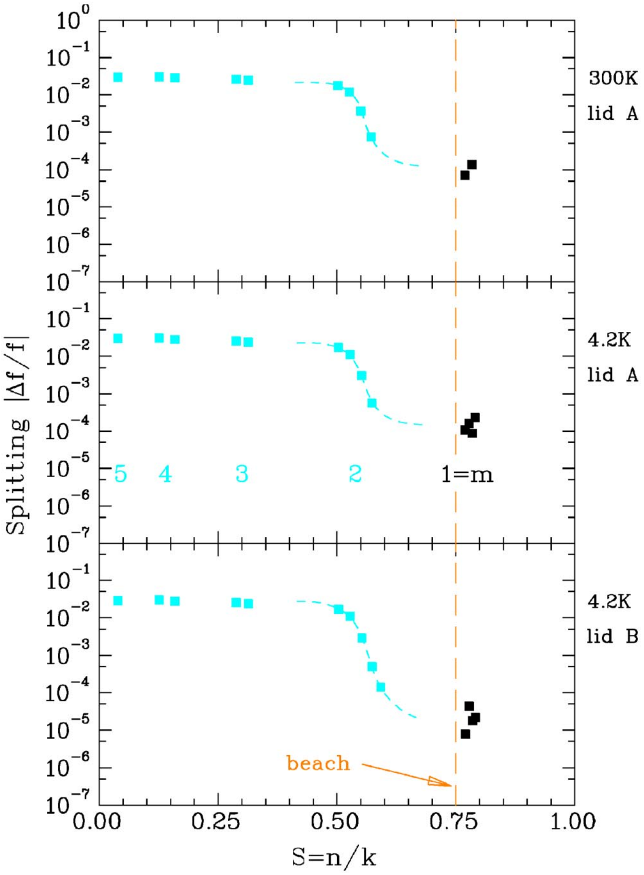

FIG. 24. (Color online) For the eccentricity $\delta=0.20$ observed splittings of quasidoublets taken from the window 8.75–10.50 GHz as a function of the quantized angular momentum S. The family $m=2$ indicates the transition (dashed curve) between chaotic (grey) and regular modes (black), respectively.

It is important to note that the exact form of the curve depends on the choice of the frequency window and the eccentricity, although the general transition behavior from chaotic to regular is universal. Two features have been observed: on the one hand, a transition at higher frequency is mediated by a family of higher radial quantum number m and, on the other hand, the position of this transition at higher eccentricities is more and more shifted towards the beach at $S=0.75$. The comparison of the three experimental conditions indicates that differences clearly manifest themselves only in the whispering gallery region—i.e., in the range of small split-

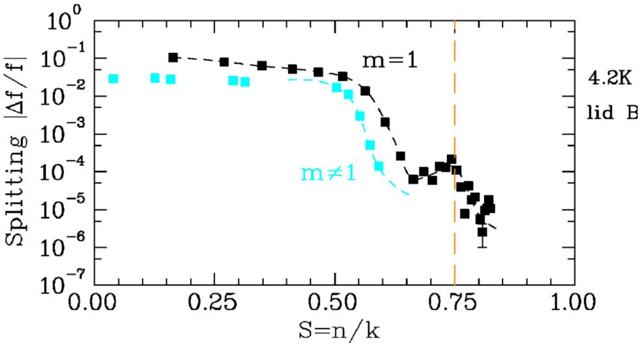

FIG. 25. (Color online) Quasidoublet splittings of the family $m=1$ (black) with angular momentum quantum numbers $n=1$–30 in the case of weakly perturbing antennas (lid B) again for $\delta=0.20$. For comparison also the modes with $m\neq 1$ (grey) from Fig. 24 (lower part) are included. Obviously, a local maximum of the family $m=1$ occurs at $S=0.75$.

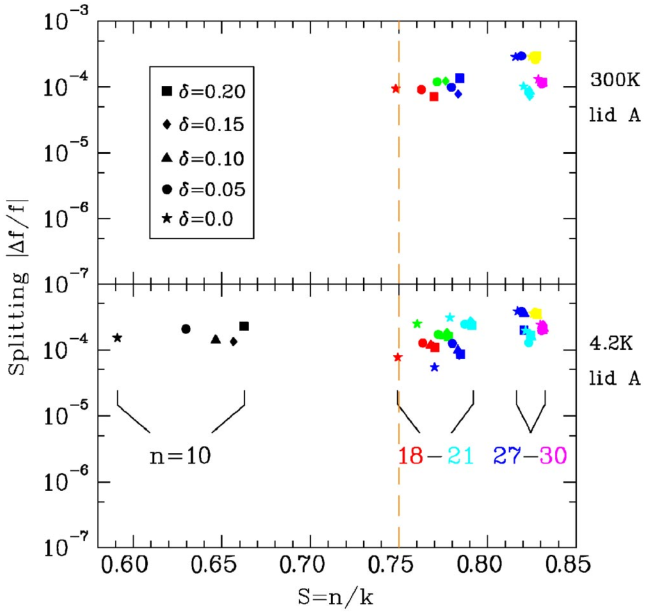

FIG. 26. (Color online) Splittings of the family $m=1$ in the zoomed-in window around $S=0.75$. The figure shows a comparison between the warm and the cold measurement, where in both cases lid *A* was used. Different symbols denote the varying eccentricity δ. Diverse grey scales have been taken for a better separation of the quasidoublets, whereby neighboring data points, all of which belonging to the same state $(n|1)$, are given in the same grey scale. The splittings of the warm measurement (300 K) fall in the range of the resolution limit for normal conducting resonator $(1/Q \gtrsim 10^{-4})$. This is also the reason for some missing data points. As a consequence of the strong perturbation of the antennas, also the points of the cold measurement (4.2 K) lie on this level (i.e., about two orders of magnitude above their resolution limit), being nearly invariant under a variation in δ.

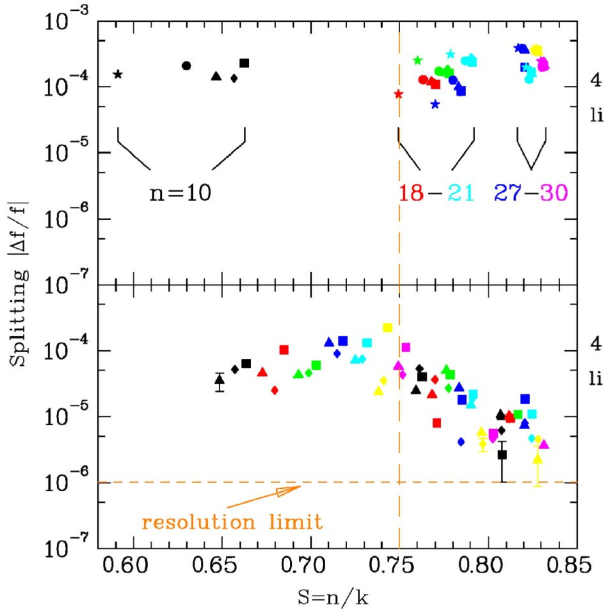

FIG. 27. (Color online) Comparison of the splittings in the superconducting state (4.2 K) using strongly (lid *A*) and weakly (lid *B*) perturbing antennas, respectively. In the latter case only three of five eccentricities were accessible. We have used the same notation as in Fig. 26. In the lower subfigure all the modes between (10|1) and (30|1) are displayed. While the upper figure shows nearly constant, perturbation-induced splittings, the lower illustration reproduces the already found maximum structure of Fig. 25 in the range around the beach at $S=0.75$. As already indicated in the theoretical prediction (see Fig. 14), also here the data points show a systematical rise in the chaotic sea $(S<0.75)$ and a fluctuating fall in the whispering gallery region $(S>0.75)$.

tings. Already at first sight, the splittings in the case of weakly perturbing antennas (lid *B*) are about one order of magnitude below the corresponding values for strongly perturbing antennas (lid *A*).

Before this behavior is studied in more detail, the transition range around $S=0.75$ will be closely inspected with respect to a significant splitting structure, which allows us not only to classify states as "chaotic" or "regular," but also accounts for the special character of the beach modes. For this purpose, Fig. 25 enlarges the lower part of Fig. 24—i.e., shows the splittings of the modes (1|1)–(30|1). Beside the typical transition behavior from chaotic to regular states (now also for $m=1$), as described above, a substructure becomes visible in the range around $S=0.75$, indicating a first piece of evidence for chaos-assisted tunneling. Here, in the direct vicinity of the beach—i.e., at the crossover between chaotic sea and whispering gallery region—the splittings reveal a very impressive *local maximum*, indeed indicating that due to the strong coupling of the two classically separated phase-space regions, the class of beach modes residing here has drastically amplified splittings—i.e., an increased tunneling probability. Independent from the tunneling itself, it is semiclassically expected that beyond this borderline in the whispering gallery region, the quasidoublet splittings become small very rapidly with increasing angular momentum as well as with increasing energy [16–20]. Beside this theoretical expectation, the experiment also shows a sharp decline *inside* the chaotic sea; therefore, semiclassical arguments are invalid and a direct correlation with an increased tunneling probability is obvious.

Especially in the region of this maximum it is now important to investigate the particular influence of the chaoticity, since the tunneling probability is a function of the coupling of the two separated whispering gallery regions and therefore directly depending on the structure of the chaotic sea (see Fig. 4). For this purpose, Figs. 26 and 27 show in detail the splittings of the whispering gallery states in the direct vicinity of the beach line at $S=0.75$. For a more systematic separation of different effects at different measuring conditions, Fig. 26 shows at first a comparison of the experiments at 300 K and 4.2 K, respectively, where in both cases strongly perturbing antennas (lid *A*) were used. In Fig. 27 the comparison of this case and the weakly perturbing antennas (lid *B*) at 4.2 K can finally be seen.

These two figures reflect another central result of the presented experiments on chaos-assisted tunneling. For a variable eccentricity δ (five different symbols for the measurements using lid *A*, three in the case of lid *B*), primarily three groups of states for the family $m=1$ are shown: the mode (10|1) inside the chaotic sea, the modes (18|1)–(21|1) near the beach line, and the modes $(27|1)$–$(30|1)$ far outside in the whispering gallery region (see also Fig. 7 for the concentric case). In addition, in the case of lid B all states between $(10|1)$ and $(30|1)$ are given in order to make clearly visible the detailed structure of the emerging local maximum. For a discrimination, the splittings of different quasidoublets are sorted by different grey scales.

Due to the resolution limit of the normal conducting resonator ($1/Q \gtrapprox 10^{-4}$), only a small fraction of the splittings can be determined from the 300-K measurement. Although the measurement at 4.2 K using the superconducting resonator with lid A allows us to record all searched splittings, it is impossible to draw any physical conclusion concerning the tunneling from that data. The reason is that all these splittings are nearly identical, showing no dependence on the frequency f, the angular momentum quantum number n, or the eccentricity δ. For comparison, see also the example of the quasidoublet $(18|1)$ of Fig. 11 (left half). Obviously, the antennas of lid A, which are mounted right inside the whispering gallery region (at $S=0.907$), lead to a perturbation-induced amplification of the splittings by two orders on magnitude with respect to the principal resolution limit of the superconducting resonator ($1/Q \gtrapprox 10^{-6}$). Therefore, the data points of both subfigures agree fairly well.

A totally different behavior occurs when lid B is used (see Fig. 27). To emphasize again, the corresponding systems of the given two subfigures only differ in the very position of their antennas. As already indicated in Fig. 25 for the eccentricity $\delta=0.20$, in using lid B a local maximum of quasidoublet splittings emerges in this region. This structure is even intensified now by the two additional eccentricities $\delta=0.10$ and $\delta=0.15$. A comparison with the theoretical prediction, as introduced in the last section, shows a fairly good agreement in the general behavior of the splittings within this window of angular momenta. Also the data points of Fig. 14 obey a distinct maximum structure around $S=0.75$ with a systematical rise in the chaotic sea and a statistical fall in the whispering gallery region. Note that after minimizing the impact of the antennas on the symmetry, the remaining imperfections of the resonator lead to a smoothing of the maximum for the experimental curve [see Fig. 27 (bottom)]. A closer inspection reveals even more agreement with the theoretical curve. Also the experimental rise of the quasidoublet splittings in the chaotic sea features a systematical behavior, which is indicated by the fact that those data points of the highest eccentricity $\delta=0.20$ represent the highest splittings for the individual quasidoublets. Additionally, splittings in both curves—the experimental and theoretical ones—show strong fluctuations in the transition to the whispering gallery region when δ is varied. As already mentioned in the theoretical framework, this is basically caused by crossings of whispering gallery quasidoublets with chaotic states [14,16]. Finally, the experimental curve also clearly displays that the accessible window for an observation of chaos-assisted tunneling was fully utilized: Only in the range of the experimental resolution limit ($1/Q \approx 10^{-6}$), which is reached by a few data points, some of the quasidoublets eventually cannot be resolved and therefore are missing even in the lower subfigure of Fig. 27. This also demonstrates how critically an observation of chaos-assited tunneling rests on the usage of superconducting resonators.

VI. QUALITY FACTORS

While the theoretical treatment of the quantum annular billiard only yields discrete eigenvalues, the experiment provides resonances with a finite width Γ (we use the FWHM). Therefore, it is very instructive to transfer the investigations on the splittings as described in the last section also to these widths in order to look for further signatures of chaos-assisted tunneling. The width of a resonance of a microwave resonator is caused by two different mechanisms: First, a fraction of the energy stored in the resonator is dissipated by Ohmic losses at the inner surfaces. Besides different kinds of high-frequency losses in the case of normal conducting and superconducting resonators, respectively, the purity of these surfaces plays the important role. The second mechanism is caused by the coupling to the resonator, which beside the excitation also takes a certain portion of energy from the system.

Formally, for a given resonance with frequency f and width Γ the connection between these two kinds of losses might be expressed in terms of the loaded quality factor Q_L and the unloaded quality factor Q_0 in the following way [61,62]:

$$Q_L = \frac{f}{\Gamma} = \frac{Q_0}{1+\beta}, \tag{11}$$

$$Q_0 = 2\pi f \frac{U_0}{P_0} = \frac{G}{R_S}. \tag{12}$$

According to this, the unloaded quality factor Q_0, which is not directly accessible in the measurement, is only determined by the properties of the resonator and the excited mode. This is expressed by the stored energy in the electromagnetic field, U_0, and the dissipated power per period, P_0, which might be converted into the geometry factor G for a constant surface resistance R_S. In contrast to this, for the loaded quality factor Q_L, which might be directly deduced from the eigenfrequency f and the width Γ, also the coupling to the field inside the resonator, which is parametrized by the coupling factor β, plays an important role. Only in the limiting case of an extremely weak coupling, $\beta \to 0$, are both quality factors identical.

In order to demonstrate that in the given experiments mainly the coupling characterizes the behavior of the systems, Figs. 28 and 29 show the loaded quality factors Q_L determined from the quasidoublets versus angular momentum. Here, for both states of a given quasidoublet with f_{even} and f_{odd}, the quality factors $Q_L^{\text{even}} = f_{\text{even}}/\Gamma_{\text{even}}$ and $Q_L^{\text{odd}} = f_{\text{odd}}/\Gamma_{\text{odd}}$ are displayed separately. Again, the sizes of the data sets of the three different measurements might differ from each other, since the numerical fitting for very weakly excited resonances may have allowed a determination of the resonance frequency but not of the resonance width. As in Figs. 26 and 27 also in the given figures, for measurements using lid A only the modes $(10|1)$ (chaotic sea), $(18|1)$–$(21|1)$ (beach), and $(27|1)$–$(30|1)$ (whispering gallery region) are plotted, while in the case of weakly perturbing antennas (lid B) all modes $(10|1)$–$(30|1)$ are given. At first sight, only the lower subfigure of Fig. 29 shows an almost exponential de-

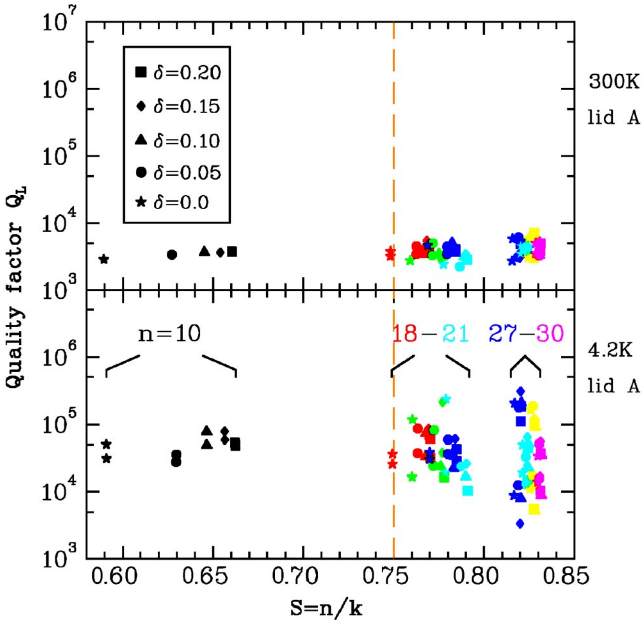

FIG. 28. (Color online) Loaded quality factors determined from the states shown in Fig. 26 at 300 and 4.2 K, respectively, using strongly perturbing antennas (lid *A*). Normally, for each quasidoublet two quality factors could be reduced (separately for the even and the odd state). Both subfigures show *on average* nearly constant quality factors as a function of the quantized angular momentum with an apparent bifurcational structure towards larger values of *S*, which is slightly present already in the normal conducting case and clearly observable in the superconducting state. The reason for this strong asymmetry in the excitation of both states of a given quasidoublet is basically composed of three effects: first, the more and more increasing localization of field distributions at higher angular momenta, and second, the nodal line structure of these fields, which is strongly correlated with the angular momentum quantum number *n*, and, third, the spatially fixed coupling to these fields.

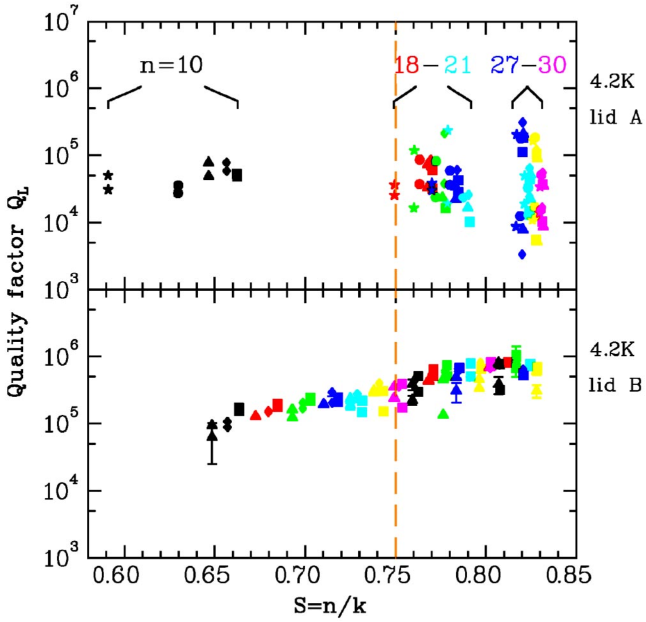

FIG. 29. (Color online) Comparison of loaded quality factors in the superconducting state (4.2 K) using strongly (lid *A*) and weakly (lid *B*) perturbing antennas, respectively. Again, per quasidoublet there are two quality factors given (which are nearly identical in the lower subfigure). In comparison to the already explained bifurcational structure for strongly perturbing antennas (upper subfigure), the lower diagram shows quality factors, nearly exponentially increasing with *S* ($\log Q_L$ linearly depends on *S*) up to the expected limit of 10^6. This nicely reflects the systematical disapproach between the antenna (located at $S=0.625$) and the balance point of the field distribution (approximately at $S=n/k$). In addition, it might be deduced from the very symmetrical excitation of both states of a given quasidoublet that indeed there is only very little impact on the mode structure by the weak coupling to the fields.

pendence between the quality factor Q_L and the quantized angular momentum *S* ($\log Q_L \propto S$) with very weak fluctuations. In contrast, among experimental conditions using lid *A* a very interesting behavior can be observed: Already slightly present in the 300 K case and much stronger at 4.2 K, the quality factors indicate *on the average* a nearly constant trend with *S*. But in considering both parities of a given quasidoublet separately, a bifurcation of the quality factors towards larger *S* can be observed. This effect is in particular obvious for the highly excited whispering gallery modes $(27|1)$–$(30|1)$ in the lower subfigure of Fig. 28. Here, the quality factors of both parities partly differ by more than one order of magnitude, confirming the direct observation on the spectrum that one state of a given quasidoublet possesses a much smaller width than the other one [see also, e.g., Fig. 11 for mode $(18|1)$ in the beach region].

From a geometrical point of view, the explanation of this behavior is straightforward and can be directly confirmed by the measured wave functions (300 K, lid *A*). Two things are important: On the one hand, the polar angle α between both antennas *A*1 and *A*2 is *constant* ($\alpha \approx 86°$). On the other hand, the polar angle $\Delta\varphi$ between two nodal lines of a given field distribution *changes* with the angular momentum quantum number *n* along a circulation around the center. Formally,

$$\Delta\varphi = \frac{360°}{2n} \qquad (13)$$

applies. Exactly the ratio of these two polar angles, $\alpha/\Delta\varphi$, is crucial for the asymmetric behavior of the resonance widths. The closer this ratio lies nearby an integer number—which means the better a fixed number of wave trains fits in between the antennas—the more effective one of the two parities will be excited (antennas in the range of a field maximum). This yields a large width and a low-quality factor, respectively. In contrast, the corresponding second parity will be excited nearly in a node of the field—i.e., very ineffectively—therefore, a small width and a high-quality factor occur. One recognizes that this leads to strongly asymmetrically distributed widths for one quasidoublet. In the inverse case, where the ratio $\alpha/\Delta\varphi$ falls exactly between two integers, both parities are excited in a similarly effective or ineffective way; thus, the corresponding quality factors are symmetrically distributed for both states of a quasidoublet. Determining the degree of asymmetry for both quality fac-

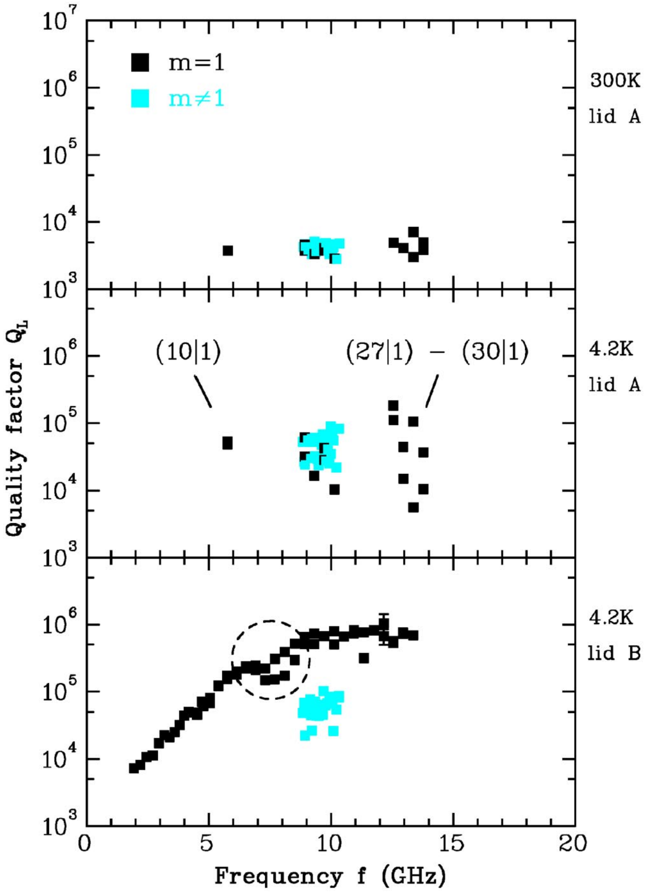

FIG. 30. (Color online) Frequency dependence of quality factors in the case of family $m=1$ (black) and $m\neq 1$ (grey), respectively, for the eccentricity $\delta=0.20$. In the lower subfigure all states (0|1)–(30|1) are considered. Here, the dashed circle marks a clearly observable minimum in the beach region.

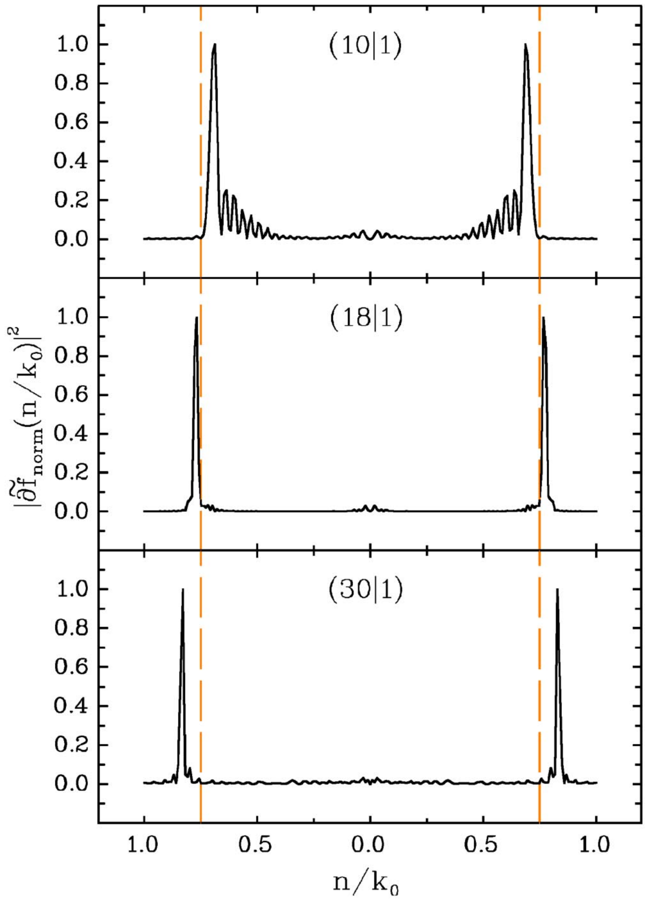

FIG. 31. (Color online) Polar Fourier transformation of the modes (10|1) from the chaotic sea, (18|1) from the beach region, and (30|1) from the whispering gallery region for the configuration $\delta=0.20$. Regular field distributions feature more and more sharply localized Fourier components beyond the beach (dashed lines).

tors in such a way yields a perfect agreement with the observations of Fig. 28 for the system with lid *A*.

In the case of field measurements at 300 K the given resolution only allows us to observe the more effectively excited parity, even though the corresponding modes produce a weakly formed double resonance, which allows us to fix two widths. Here, states with an even parity are found exactly when $\alpha/\Delta\varphi$ falls in the close vicinity of an even integer. In return, an odd state is to be observed exactly when $\alpha/\Delta\varphi$ is close to an odd integer. Again, this behavior clearly reflects how strongly the system is perturbed by the antennas of lid *A*. In substantial contrast to this, the quality factors in case of lid *B* show in general an almost identical formation for both parities of a quasidoublet [see Fig. 29 (bottom)]. Furthermore, the exponential decrease of the resonance widths with S indicates that the perturbation by the antennas (located at $S=0.625$) becomes weaker and weaker such that especially in the case of highly excited whispering gallery states the coupling to the field is nearly free of an influence on the quality factor. Formally, the coupling factor β steadily decreases and the influence of the excitation disappears,

$$\beta \rightarrow 0 \text{ and } Q_L \rightarrow Q_0. \tag{14}$$

Exactly for this reason, the splittings of the states are almost free of perturbations by the antennas; hence, their origin is based on chaos-assisted tunneling.

In order to verify the frequency dependence of the quality factors in a last step, Fig. 30 shows again for the eccentricity $\delta=0.20$ (compare Fig. 25), beside the modes from Figs. 28 and 29 of the family $m=1$, also additional states taken from the window 8.75–10.50 GHz. In the case of weakly perturbing antennas all the modes (0|1)–(30|1) are considered. Here, the two upper subfigures nicely demonstrate again that, although the quality factors strongly diverge due to the discussed asymmetry of excitation, their mean formation remains nearly constant. Furthermore, the quality factors of the states $m\neq 1$ within the window 8.75–10.50 GHz show a similar behavior as the ones of the family $m=1$, simply because both classes are affected by the geometry of the excitation in the same way, whereas in the case of weakly perturbing antennas (lower subfigure) the quality factors of these two classes are separated by more than one order of magnitude. This huge gain in lifetime [35] allows us, on the one hand, to identify easily the states of the family $m=1$ directly in the spectrum (even *without* measuring the corresponding wavefunction). On the other hand, here a natural classification with respect to chaotic, beach, and regular modes also directly emerges from the quality factors. In particular the family $m=1$ passes through all three kinds of states in the figure. Thus, from the quality factor representation [Fig. 30 (bottom)], as well as from the splitting representation (Fig. 25), a very steady transitional behavior arises.

In the picture of quality factors it also becomes very obvious what happens in the region of the discussed resolution limit of $1/Q \approx 10^{-6}$. At the end, the field strength maximum reaches a more and more fixed position within the geometry for an increasing angular momentum quantum number n; therefore, also its distance from the antennas becomes constant. Thus, the almost exponential dependence between this distance and the loaded quality factor ($\log Q_L \propto S$) [as found in Fig. 29 (bottom)] just leads in frequency representation to the observable, slowly forming saturation of the quality factors in the whispering gallery region [see Fig. 30 (bottom)].

It is rather speculative whether the *maximum* of quasidoublet splittings at $S=0.75$, which was equated with the experimental evidence of chaos-assisted tunneling for the beach modes, now appears in the form of a *minimum*, as observable on the branch of quality factors for the family $m=1$ (dashed circle in Fig. 30). Analytically, the quantized angular momentum of the centroid of this minimum gives $S\approx 0.73$. The physical interpretation of this minimum could be that the particularly effective coupling of the beach modes to the chaotic sea provides a wider smearing of the corresponding wave functions across the whole billiard than for modes just outside the minimum, where the coupling is effectively weaker. On the other hand, the stronger a wave function is smeared across the billiard—i.e., delocalized—the more "is seen" of the dissipative parts of the surface. Therefore, it might be expected that beach modes not only display larger splittings but also smaller quality factors, as observed in the experiment.

VII. POLAR FOURIER TRANSFORMATION

To visualize this smearing of states in angular momentum space, Fig. 31 exemplary contrasts the polar Fourier transformations [63] of mode $(10|1)$ (chaotic sea), of mode $(18|1)$ (beach region), and of mode $(30|1)$ (whispering gallery region) again for the configuration $\delta=0.20$. Formally, this was obtained by Fourier transforming the experimental frequency shift ∂f as taken from the field distribution measurements [compare Eq. (9)] along circles of radius ρ_0 around the origin, respectively

$$\widetilde{\partial f}(\rho_0,k) = \int_{b_{min}=-\pi\rho_0}^{b_{max}=+\pi\rho_0} db\,\partial f(\rho_0,b)\exp(ibk). \qquad (15)$$

Here, the variable $b=\rho_0\varphi$ characterizes the polar arc length. A subsequent averaging across all radii ρ_0, normalization to a maximum amplitude of unity and rescaling of the k axis to the quantized angular momentum $S=n/k_0$, with $k_0=$being the present eigenvalue,

$$\widetilde{\partial f}_{\mathrm{norm}}\left(\frac{n}{k_0}\right) = \left\langle \widetilde{\partial f}\left(\rho_0, \frac{n}{k_0} = \frac{\rho_0}{2k_0}k\right)\right\rangle_{\rho_0}, \qquad (16)$$

finally yields the curves as given in Fig. 31.

From this, it becomes quite obvious that the beach mode $(18|1)$ provides a real coupling between the chaotic sea and the whispering gallery region. In contrast, the modes $(10|1)$ and $(30|1)$ are localized only inside one of these two subregions. The figure also nicely points up how the information about the corresponding angular momentum quantum number n is encrypted in the wave function of a certain mode and "how good" this quantum number is. This can be seen from calculating the expected quantized angular momentum of a given state according to $S=n/k_0$: Right at this position the polar Fourier transform yields a maximum. Furthermore, the higher the quantum number n, the sharper the corresponding peak and also the better the agreement of its position with S. This demonstrates in the Fourier space of the wave functions how widely smeared chaotic states with "bad" quantum numbers n [mode $(10|1)$] transform into regular states with "good" quantum numbers n [mode $(30|1)$] at higher angular momentum. Thus, besides the splittings and quality factors this reveals a third observable for the chaoticity of a state, yielding again for the beach modes a significant structure in the direct vicinity of the crossover at $S=0.75$.

VIII. CONCLUSION

This work deals with new features of the relation between a classical system and the spectrum of its quantum counterpart. The two-dimensional annular billiard of the family $r+\delta=\mathrm{const}$ has a mixed phase space, containing two separated regular regions and a chaotic sea with a stable island. In the quantum analog system, the regular regions are coupled to the chaotic sea, and in this way they are coupled to each other. This causes a splitting of the doublets of eigenstates that correspond to the classical whispering gallery trajectories: This is referred to as chaos-assisted tunneling. Experimentally, these quasidoublets were measured with a very high resolution using a superconducting resonator and were subsequently identified via electromagnetic field distributions of a normal conducting twin resonator. In this way, chaos-assisted tunneling was observed experimentally for the first time. In this observation, the so-called beach modes—which correspond to the orbits on the border of the chaotic sea—played a major role. The beach modes show a maximum of doublet splitting. This indicates a maximum of tunneling probability at the border of the chaotic sea. In addition to the splitting, we investigated resonance widths and found a weak maximum of the widths at the beach modes. This amounts to enhanced dissipation and is explained by the fact that these modes are coupled to trajectories all over the billiard via their coupling to the chaotic states.

ACKNOWLEDGMENTS

We are particularly grateful to O. Bohigas for encouraging us to study this novel mechanism of tunneling and him as well as S. Tomsovic and D. Ullmo for their kind invitations to Orsay and many fruitful discussions. We thank E. Doron and S. Frischat for many calculations and especially for guiding us to "look on the beach." We are also grateful to R. Egydio de Carvalho for providing us with numerical data and to D. Boosé for his interest in our experiments. We would also like to thank H. Lengeler for numerous hints on field strength measurements at high frequencies. This work has been supported by the Deutsche Forschungsgemeinschaft (DFG) under Contract Nos. SFB 185, Ri 242/16, and SFB 634.

[1] C. Dembowski, H.-D. Gräf, A. Heine, R. Hofferbert, H. Rehfeld, and A. Richter, Phys. Rev. Lett. **84**, 867 (2000).

[2] W. K. Hensinger, H. Häffner, A. Browaeys, N. R. Heckenberg, K. Helmerson, C. McKenzie, G. J. Milburn, W. D. Phillips, S. L. Rolston, H. Rubinsztein-Dunlop, and B. Upcroft, Nature (London) **412**, 52 (2001).

[3] D. A. Steck, W. H. Oskay, and M. G. Raizen, Science **293**, 274 (2001).

[4] D. A. Steck, W. H. Oskay, and M. G. Raizen, Phys. Rev. Lett. **88**, 120406 (2002).

[5] A. Mouchet and D. Delande, Phys. Rev. E **67**, 046216 (2003).

[6] D. Delande and J. Zakrzewski, Phys. Rev. A **68**, 062110 (2003).

[7] W. K. Hensinger, N. R. Heckenberg, G. J. Milburn, and H. Rubinsztein-Dunlop, J. Opt. B: Quantum Semiclassical Opt. **5**, R83 (2003).

[8] W. K. Hensinger, A. Mouchet, P. S. Julienne, D. Delande, N. R. Heckenberg, and H. Rubinsztein-Dunlop, Phys. Rev. A **70**, 013408 (2004).

[9] M. J. Davis and E. J. Heller, J. Chem. Phys. **75**, 246 (1981).

[10] M. Wilkinson, Physica D **21**, 341 (1986).

[11] O. Bohigas, S. Tomsovic, and D. Ullmo, Phys. Rev. Lett. **64**, 1479 (1990).

[12] O. Bohigas, S. Tomsovic, and D. Ullmo, Phys. Rev. Lett. **65**, 5 (1990).

[13] O. Bohigas, S. Tomsovic, and D. Ullmo, Phys. Rep. **223**, 43 (1993).

[14] S. Tomsovic and D. Ullmo, Phys. Rev. E **50**, 145 (1994).

[15] F. Leyvraz and D. Ullmo, J. Phys. A **29**, 2529 (1996).

[16] O. Bohigas, D. Boosé, R. Egydio de Carvalho, and V. Marvulle, Nucl. Phys. A **560**, 197 (1993).

[17] E. Doron and S. D. Frischat, Phys. Rev. Lett. **75**, 3661 (1995).

[18] E. Doron and S. D. Frischat, J. Phys. A **30**, 3613 (1997).

[19] E. Doron and S. D. Frischat, Phys. Rev. E **57**, 1421 (1998).

[20] S. D. Frischat, Ph.D. thesis, Universität Heidelberg, 1996.

[21] P. Gerwinski and P. Šeba, Phys. Rev. E **50**, 3615 (1994).

[22] R. Roncaglia, L. Bonci, F. M. Izrailev, B. J. West, and P. Grigolini, Phys. Rev. Lett. **73**, 802 (1994).

[23] A. Shudo and K. S. Ikeda, Phys. Rev. Lett. **74**, 682 (1995).

[24] O. Brodier, P. Schlagheck, and D. Ullmo, Phys. Rev. Lett. **87**, 064101 (2001).

[25] A. Mouchet, C. Miniatura, R. Kaiser, B. Grémaud, and D. Delande, Phys. Rev. E **64**, 016221 (2001).

[26] R. Artuso and L. Rebuzzini, Phys. Rev. E **68**, 036221 (2003).

[27] T. Onishi, A. Shudo, K. S. Ikeda, and K. Takahashi, Phys. Rev. E **68**, 056211 (2003).

[28] W. Greiner, *Quantum Mechanics, An Introduction*, 4th ed., (Springer, Berlin, 2000).

[29] A. Messiah, *Quantum Mechanics* (Dover, New York, 2000).

[30] C. A. Stafford and B. R. Barrett, Phys. Rev. C **60**, 051305 (1999).

[31] J. U. Nöckel and A. D. Stone, Nature (London) **385**, 45 (1997).

[32] J. U. Nöckel and A. D. Stone, in *Optical Processes in Microcavities*, edited by R. K. Chang and A. J. Campillo (World Scientific, Singapore, 1996).

[33] S. Åberg, Phys. Rev. Lett. **82**, 299 (1999). Note, however, in our opinion the term "chaos-assisted tunneling" has here been used in a different physical situation.

[34] A. Richter, in *Emerging Applications of Number Theory, The IMA Volumes in Mathematics and its Applications*, Vol. 109, edited by D. A. Hejhal, J. Friedman, M. C. Gutzwiller, and A. M. Odlyzko (Springer, New York, 1999), p. 479.

[35] G. Hackenbroich and J. U. Nöckel, Europhys. Lett. **39**, 371 (1997).

[36] M. Hentschel and K. Richter, Phys. Rev. E **66**, 056207 (2003); M. Hentschel, Ph.D. thesis, TU Dresden, 2001.

[37] M. V. Berry and M. Wilkinson, Proc. R. Soc. London, Ser. A **392**, 15 (1984).

[38] M. V. Berry, Eur. J. Phys. **2**, 91 (1981).

[39] H. G. Schuster, *Deterministic Chaos*, 2nd revised ed. (VCH, Weinheim, 1988).

[40] M. Tabor, *Chaos and Integrability in Nonlinear Dynamics* (Wiley, New York, 1989).

[41] E. Ott, *Chaos in Dynamical Systems* (Cambridge University Press, Cambridge, England, 1993).

[42] D. Boosé (private communication).

[43] H.-J. Stöckmann, *Quantum Chaos: An Introduction* (Cambridge University Press, Camebridge, England, 1999).

[44] O. Bohigas (private communication).

[45] L. C. Maier, Jr. and J. C. Slater, J. Appl. Phys. **23**, 68 (1952).

[46] S. Sridhar, D. O. Hogenboom, and Balam A. Willemsen, J. Stat. Phys. **68**, 239 (1992).

[47] A. Gokirmak, D. H. Wu, J. S. A. Bridgewater, and S. M. Anlage, Rev. Sci. Instrum. **69**, 3410 (1998).

[48] D. H. Wu, J. S. A. Bridgewater, A. Gokirmak, and S. M. Anlage, Phys. Rev. Lett. **81**, 2890 (1998).

[49] C. Dembowski, H.-D. Gräf, R. Hofferbert, H. Rehfeld, A. Richter, and T. Weiland, Phys. Rev. E **60**, 3942 (1999).

[50] U. Dörr, H.-J. Stöckmann, M. Barth, and U. Kuhl, Phys. Rev. Lett. **80**, 1030 (1998).

[51] R. Egydio de Carvalho (private communication).

[52] H. P. Baltes and E. R. Hilf, *Spectra of Finite Systems* (Bibliographisches Institut AG, Zürich, 1976).

[53] C. Dembowski, H.-D. Gräf, A. Heine, H. Rehfeld, A. Richter, and C. Schmit, Phys. Rev. E **62**, R4516 (2000).

[54] E. J. Heller, Phys. Rev. Lett. **53**, 1515 (1984).

[55] E. J. Heller, Lect. Notes Phys. **263**, 162 (1986).

[56] E. B. Bogomolny, Physica D **31**, 169 (1988).

[57] H. Alt, P. von Brentano, H.-D. Gräf, R.-D. Herzberg, M. Phil-

ipp, A. Richter, and P. Schardt, Nucl. Phys. A **560**, 293 (1993).
[58] H. Alt, P. von Brentano, H.-D. Gräf, R. Hofferbert, M. Philipp, H. Rehfeld, A. Richter, and P. Schardt, Phys. Lett. B **366**, 7 (1996).
[59] M. Philipp, Ph.D. thesis, Universität zu Köln, 1997.
[60] F. Beck, C. Dembowski, A. Heine, and A. Richter, Phys. Rev. E **67**, 066208 (2003).
[61] CERN Accelerator School (Hamburg, 1988), edited by S. Turner, CERN 89-04, 1989.
[62] CERN Accelerator School (Oxford, 1991), edited by S. Turner, CERN 92-03, 1992.
[63] E. Doron and S. D. Frischat (private communication).